Full-scale testing of naturally buckling steel braces and evaluation of partially rib-strengthened sections to cumulative damage

Hayashi, Kazuhiro; Skalomenos, Konstantinos; Jamshiyas, Shadiya; Inamasu, Hiroyuki

[Link to publication on Research at Birmingham portal](#)

FULL-SCALE TESTING OF NATURALLY BUCKLING STEEL BRACES AND EVALUATION OF PARTIALLY RIB-STRENGTHENED SECTIONS TO CUMULATIVE DAMAGE

Kazuhiro Hayashi[a], Konstantinos A. Skalomenos[b,*], Shadiya Jamshiyas[b], Hiroyuki Inamasu[c]

[a] Assistant Professor
Department of Architecture and Civil Engineering, Toyohashi University of Technology
1-1 Tempaku-cho, Toyohashi, Aichi 441-8580, Japan

[b] Assistant Professor
Department of Civil Engineering, University of Birmingham
Edgbaston, Birmingham, B15 2TT, United Kingdom

[b] PhD Student
Department of Civil Engineering, University of Birmingham
Edgbaston, Birmingham, B15 2TT, United Kingdom

[c] Doctoral Assistant
School of Architecture, Civil and Environmental Engineering,
Ecole Polytechnique Federale de Lausanne (EPFL)
Lausanne CH-1015, Switzerland.

Abstract. Naturally buckling steel braces (NBBs) have been recently developed by the authors and co-workers to improve the buckling performance and energy dissipation capacity of braced framed structures. In NBBs, a low-yield-point steel (LYS) channel and a high-strength steel (HSS) channel are connected using steel battens to build up a dual-material steel section. An intentional eccentricity is introduced along the brace length to subject the brace to bending loads in addition to axial loads. Previous experiments have demonstrated that this combined axial-flexural response stabilizes the compression behaviour of the brace and enhances its tensile post-yielding stiffness through a novel deformation mechanism. In this paper, the cyclic behaviour of two full-scale NBB specimens with different section sizes and eccentricities are investigated experimentally. Gusset plate pin-connections that accommodate in-plane buckling are used to release the brace ends from high ductility demands. Two low-cycle fatigue protocols with increasing amplitudes and repeated inelastic loading cycles at the event of local buckling are adopted. Test results show that both NBB specimens exhibited a stable hysteresis behaviour by delaying the onset of local buckling up to a 1.5 % story drift ratio (SDR). Notably, the specimen with larger section and larger eccentricity provided a stable tensile strength under five repeated loading cycles of 2.0 % SDR. An equivalent damping ratio of 0.4 was measured. In addition to the experimental research, a computational study is performed with the aid of the finite element software ABAQUS to evaluate partially strengthening method of the sections against local buckling. It was found that the energy dissipation capacity of NBBs can be enhanced up to 40% by using rib stiffeners at critical locations, while the use of thicker channel battens can provide further restrain to local buckling growth up to a 3.0% SDR. The paper develops the physical equations to support an analytical hysteretic model for predicting the force-displacement cyclic relationship of chevron NBBs. The accuracy and targeted conservatism of the proposed hysteretic model is confirmed through comparisons with the test results.

*Corresponding author: Dr Konstantinos Skalomenos, Email: k.skalomenos@bham.ac.uk

1. Introduction

Steel braces are often used as vertical and lateral load resistant systems in multi-story buildings for dissipating large amount of input energy when structures are subjected to damaging dynamic loads, such as strong winds and earthquakes. While the most frequently used Concentrically Braced Frames (CBFs) configured by conventional steel braces increase the lateral stiffness of steel framed structures and decrease the lateral story drift, they exhibit a marked strength deterioration under large compression loads followed by a limited deformation ductility capacity. Even though CBFs are characterized by simple configuration and relatively low fabrication cost [1-4], quite large steel sections are required to satisfy global and local buckling limits in addition to strength requirements. New bracing systems are under development with controlled inelastic behaviour providing a better satisfaction of design objectives [5-7].

Buckling Restrained Braced Frames (BRBFs) have been proved to be a reliable alternative to CBFs overcoming some of the deficiencies mentioned above. Since the inner steel core of Buckling Restrained Braces (BRBs) is laterally supported and restrained from buckling by the outer steel/concrete casing, their performance under compression is not limited by buckling, thus smaller yielding sections can be used unlike their conventional brace counterpart [8-11]. BRBs provide relatively large strength and stiffness under both tension and compression loads. They exhibit a stable hysteretic behaviour without strength deterioration after many loading cycles by controlling global buckling efficiently as well as local buckling to an extent. However, their fabrication requires strong and heavy buckling restrainers, which in turn increase the weight of the structures. In both CBFs and BRBFs, residual story displacements, and in a worst-case loading scenario, a soft-story failure mechanism may occur under rare earthquake events, which is resulted by their inherent low post-yielding stiffness [12-14].

Recently, the authors and co-workers developed an alternative brace known as Naturally Bucking Brace (NBB) [15-18] with the goal to eliminate the above drawbacks. The main advantages of NBBs are: (1) the relatively high tensile post-yielding stiffness, (2) the delay of mid-length local buckling, thereby fracture, without using external buckling restraints or large steel sections, and (3) the multiple yielding strengths combined with an axial-flexural behaviour that are useful to satisfy multiple seismic performance objectives. NBB consists of a built-up dual-material steel section made of a low-yield-point steel (LYS) channel and a high-strength steel (HSS) channel arranged in parallel and joined together through a series of battens that secure transfer of the internal forces and compactness of the section. An intentional eccentricity is introduced along the brace length that inherently subjects the brace to bending loads in addition to axial loads [19]. The effective combination of the two steel grades (i.e., large material contrast) and eccentricity helps the brace to develop a stable and advantageous hysteretic behaviour. Recent works [20, 21] have focused on slenderness effects of the NBBs under seismic loads and effects of far-field and near-fault cyclic loads on seismic performance of braces demonstrating their efficiency in various built-up rectangular steel sections and chevron configurations. The design concept of the combined axial-flexural behaviour of braces has also been recently validated in uniform circular steel sections where the target material contrast was achieved by utilizing the induction-heat treatment technology for the one half of the section [22, 23].

To incorporate the real-life scenario and understand the actual time of events occurring under seismic loads, this study adopted full-scale specimens for investigation unlike the previous works on NBB [15-18]. This is done deliberately keeping in mind the size effect in specimens and its effect on performance evaluation indices of the test. There are enough evidences in the literature which discusses scaling effect in structural specimens [24-26]. Their results showed that the drift capacity reduces with increasing specimen size. Local buckling can be initiated in larger scale specimens at lower drift levels compared to small scale specimens. Initiation of local buckling weakens the steel section and suddenly reduces the load carrying capacity of the member. Thus, this phenomenon should be prevented or delayed ensuring the safety and serviceability of structures.

Reverse cyclic loading experiments conducted on various types of special CBF braces in [27] by considering the use of more compact sections, steel pipes or wide-flange sections and concrete-filled pipes to prevent local buckling at even extremely large drifts. Researches on strengthening of BRBFs suggested local buckling reduction in H-section steel-core BRBs with a stopper in the middle of core member and gradual change of cross-section of core plate [28], local buckling restraint conditions for various tube restrainer configurations in BRBs under cyclic loading [29]. Various studies explored the use of stiffeners to resist local buckling in different steel sections and it was found to be an effective way. Mulligan and Pekoz [30] who investigated the effect of edge stiffeners in lipped channel sections found a significant improvement in the local-buckling resistance. Further works suggested enhancing local-buckling resistance through selecting optimum stiffener position and proportion for web stiffeners [31], appropriate size of stiffeners for stiffened plates [32] and proper configuration and sectional sizes for longitudinal stiffeners in case of bolted side plated beams [33]. As local buckling is observed in LYS channel of NBBs, strengthening of NBBs by partially utilizing rib stiffeners in the critical zones of the brace or increasing the thickness of channel battens to enhance stiffness locally is explored in this study. The use of rib stiffeners appears to be a quite straightforward strengthening approach for NBBs, as they consist of open channel steel sections and there is low possibility of complications in placement, accessibility and weldability of the ribs.

The authors, in their previous studies, introduced the concept of NBB and conducted the proof-of-concept investigation by subjecting reduced-scale NBB specimens to cyclic loading using mechanical pins as an "ideal" connection detail that secures the free bending of brace body. Under such ideal boundary conditions, the beneficial behaviour of the combined axial-flexural behaviour of NBB was validated. In this paper, by targeting the wider application of NBBs in real-world structures, the cyclic performance of NBBs is experimentally investigated using (a) full-scale test specimens and (b) gusset-plate connections that are widely used in practice. Gusset plates are designed to behave as pin connections [34, 35] allowing the free rotation of the brace ends in-plane of the frame, thus reducing the already increased strain demands at brace ends due to bending [23]. The influence of the section size of the brace on its energy dissipation capacity is evaluated. Then, a detailed finite element analysis study is performed to calibrate the computational model with the experimental results which are found to be in good agreement. Additional detailed finite element models with rib stiffeners and stronger channel battens are developed in order to perform a parametric study focusing on the effectiveness of such strengthening methods in eliminating the local buckling related failures. The effect of several parameters, such as, the number and thickness of stiffening ribs as well as the thickness of channel battens is examined. Finally, physics-based mathematical formulae are proposed to support the development of the hysteretic analytical model of NBBs which in turn is validated with the full-scale test results. As a result, one can use the proposed hysteretic model for the direct simulation of NBBs alone or as members of framed structures to determine their response to cyclic/seismic loading [36].

2. Basic characteristics of NBB

2.1. Configuration of NBB

As shown in Fig. 1, NBB consists of two cold-formed low-yield-point steel (LYS) and high-strength steel (HSS) channels connected along the brace length at multiple points. In this paper, steel battens are welded to each channel as shown in Fig. 1. The dotted line in the figure indicates the line of action of force. The brace-ends are free to rotate about x-axis while are fixed to rotate about y-axis.
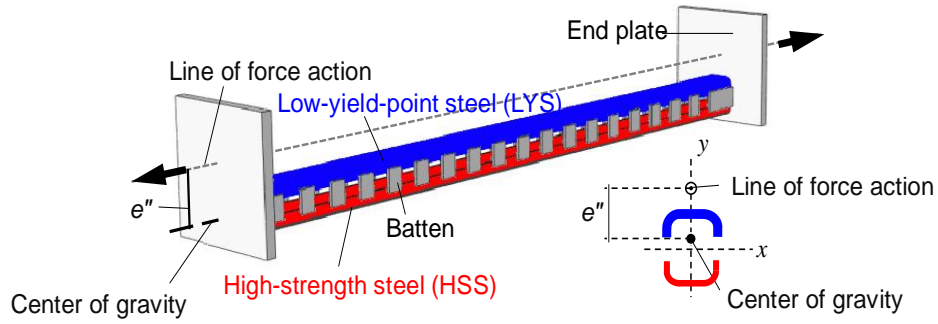
Fig. 1. Overview of Naturally Buckling Brace

LYS exhibits a low yielding stress (120~220MPa) and a high inelastic deformation capacity (30~50%) which bonuses the overall ductility of NBB. On the other hand, HSS exhibits a high yielding stress (600~800MPa) which bonuses the overall strength of NBB, but emphasis needs to be given in the lower ductility (10~15%) of HSS. In NBB configuration, the presence of eccentricity redistributes the internal stresses in a way that HSS maintains elasticity for very large inelastic deformations. At the same time, the very high ductility of LYS is efficiently exhausted. This configuration eventually contributes to the high post-yielding stiffness of NBBs inherently supported by this contrast of the material properties. The bending moment due to the presence of eccentricity acts in a different direction under tensile and compressive axial forces. Under cyclic loading, unlike the unstable phenomenon of the axial buckling, NBB bends stably due to this combined axial-flexural behaviour [15-19].

2.2 Backbone equations of NBB

NBB exhibits different behaviour in tension and compression. Fig. 2 illustrates the backbone curve of the brace. The backbone curve of NBB is approximated by a trilinear line in tension and a bilinear line in compression. In tension, the elastic range is defined until yielding of LYS channel. The tensile post-yielding stiffness is the stiffness defined beyond yielding of LYS until the yielding of HSS channel. The range beyond yielding of HSS channel is defined as the hardening stiffness range.
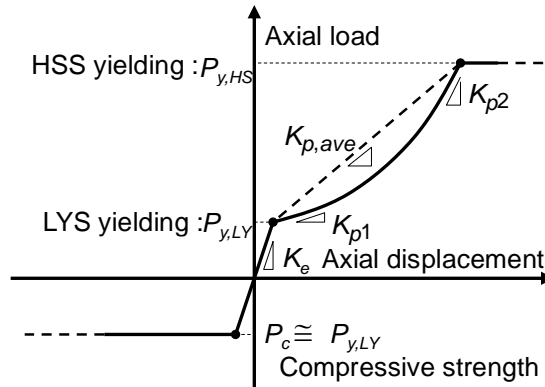

Fig. 2. Backbone of Naturally Buckling Brace

Due to the original geometrical shape of NBB, as shown in Fig. 1, the initial stiffness is uncoupled from the yielding strength due to the combined axial-flexural behaviour. The elastic stiffness K_e of NBB includes both the effect of axial force and bending moment and is expressed by the following equation [15, 17]:

$$K_e = \frac{E(A_{LY} + A_{HS})/L}{1 + (e''/r_{com})^2} \tag{1}$$

The axial load corresponding to the yielding of LY steel channel $P_{y,LY}$ (Fig. 2) is estimated as the load at which the first fiber of the LYS channel yields [14]:

$$P_{y,LY} = \frac{\sigma_{y,LY}(A_{LY} + A_{HS})}{1 + e''(A_{LY} + A_{HS})/S_{com}} \tag{2}$$

In Eqs. (1) and (2), E is the Young's modulus of the steel material, A_{LY} and A_{HS} are the cross-sectional area of the LYS and HSS channels, respectively, L is the pin-to-pin effective brace length, e'' is the applied initial eccentricity (Fig. 1), r_{com} and S_{com} are the radius of gyration and the elastic section modulus of the entire NBB section about x-axis (Fig. 1), $\sigma_{y,LY}$ is the yield stress of the LYS.

In the range beyond yielding of the LYS channel (defined as post-yielding range), a certain part of the built-up section does not contribute to the post-yielding stiffness because part of the section has yielded. The unyielded portion of the built-up section is mainly the HSS channel and is called hereafter as the "effective section". Considering this, the post-yielding stiffness right after yielding of LYS channel, K_{p1} (see Fig. 2), can be estimated by employing Eq. (3), which is a modified version of Eq. (1). In this modified version, as eccentricity (e) is defined as the distance of the HSS channel centroid with respect to the line of the force action. A reduction factor for the radius of gyration (C_1) is also introduced which is explained later. Thus, the equation K_{p1} is as follows:

$$K_{p1} = \frac{EA_{HS}/L}{1 + \{e/(C_1 r_{com})\}^2} \tag{3}$$

The post-yielding stiffness gradually increases from the initial value, K_{p1} (governed mainly by the flexural stiffness), to the final value, K_{p2} (governed mainly by the axial stiffness), as the tensile axial displacement increases (Fig. 2). This happens due to the gradual increase of the axial stiffness which becomes predominant until the brace reaches the straight configuration in the middle length ($e \approx 0$) followed by the full yielding of the HSS channel (Fig. 2). The axial-governed post-yielding stiffness, K_{p2}, is estimated by employing Eq. (4) which considers a second effective eccentricity reduction factor C_2 as follows:

$$K_{p2} = \frac{EA_{HS}/L}{1 + \{C_2 e/(C_1 r_{com})\}^2} \tag{4}$$

Finally, the overall post-yielding stiffness of the brace is simplified as a linear approximation of the nonlinear post-yielding stiffness and can be estimated as the average of K_{p1} and K_{p2}:

$$K_{p,ave} = (K_{p1} + K_{p2})/2 \tag{5}$$

The effective factors (C_1 and C_2) were originally introduced in Ref. [15]. Inamasu et al. [18] performed numerical parametric simulations of NBBs subjected to monotonic loading in which the ratio between the yield stresses of LYS and HSS, the initial eccentricity, the brace length, the width of LYS and HSS channels, and the distance between the channels were investigated. The results suggested that the factors C_1 and C_2 can be expressed as follows:

$$C_1 = \{-0.0045(e''/r_{com}) + 0.024\}(L/r_{com}) \tag{6}$$

$$C_2 = \{-0.45(e''/r_{com}) + 1.75\}(\sigma_{y,HS}/\sigma_{y,LY})^{-0.5} \tag{7}$$

Beyond yielding of the HSS, the entire built-up section of the NBB is yielded. At this ultimate stage, the center of rigidity of the NBB section (i.e., center of gravity line) is coincided with the line of force action, thus the eccentricity at this stage can be taken equal to zero. Therefore, the ultimate strength of the NBB, $P_{y,HS}$ (see Fig. 2) is taken as:

$$P_{y,HS} = \sigma_{u,LY}A_{LY} + \sigma_{y,HS}A_{HS} \tag{8}$$

where $\sigma_{u,LY}$ is the ultimate tensile stress of the LYS. The ultimate tensile stress is adopted for LYS considering that LYS experiences considerable amount of inelastic strains at this stage [15, 17].

In compression, the elastic stiffness K_e of NBB can be considered the same as in tension (Eq. (1)). Once the LYS channel experiences yielding, the deflection of the brace mid-length further increases enlarging the second order effects of the member (P-δ). The flexural-governed compression post-yielding stiffness brings the brace into its post-buckling region skipping the development of the critical buckling load. Therefore, the compressive strength of the NBB is governed by in-plane elasto-plastic instability approximated by employing Eq. (2):

$$P_c \cong P_{y,LY} \tag{9}$$

3. Testing of full-scale NBB specimens

3.1. Overview of the test specimens

To evaluate the seismic performance of the full-scale NBBs, a quasi-static cyclic testing is performed. Two specimens, the Specimen 1 and the Specimen 2, are fabricated. Their design details are summarized in Table 1 and Fig. 3. Both specimens are designed in chevron configuration (45° angle) to provide a lateral strength equal to 900 - 1000kN at a 1.0% lateral story drift ratio (SDR). This was achieved by adjusting the intentional eccentricity and cross-sectional area accordingly. Specimen 1 is designed to reach its maximum strength $P_{y,HS}$ at a 4.0% SDR. Assuming that the design drift level is around at a 2.0% SDR, 4.0% is considered adequate for the maximum allowable deformation. It is noted that this assumption is almost equivalent to the reference specimen (HLS-D20-E60) tested by the authors and co-workers in Ref. [15] (details of this specimen are included in Table 1). While comparing Specimen 1 and HLS-D20-E60, the size-effect exists. On the other hand, the Specimen 2 is designed to reach its maximum strength at 8% SDR. In Specimen 2, a higher ductility is expected due to larger cross-section and eccentricity than those of Specimen 1.

In this study, the Japanese steels SM570 and LY225 are used for the fabrication of HSS and LYS channels, respectively. Fig. 4 shows the tensile coupon test results of those steel materials. 9mm-thick HSS and a 12mm-thick LYS steel plates are used to fabricate the cold-formed channels. For cold-forming, the interior and exterior radius should be equal to one time and two times the plate thickness, respectively. By using a thicker plate for LYS channel, a better energy dissipating performance is expected. The channel battens are made of SS400 steel of 5 mm thickness for Specimen 1 and 7 mm thickness for Specimen 2. The steel battens are welded to the surface of each channel flanges through fillet welding. The end plates are welded to brace ends through complete joint penetration welding. It is noted that in Specimen 1 the thickness of battens, t_Batten was equal to 6 mm, while in Specimen 2, was equal to 9 mm.

Table 1 Dimensions and material properties of test specimens.

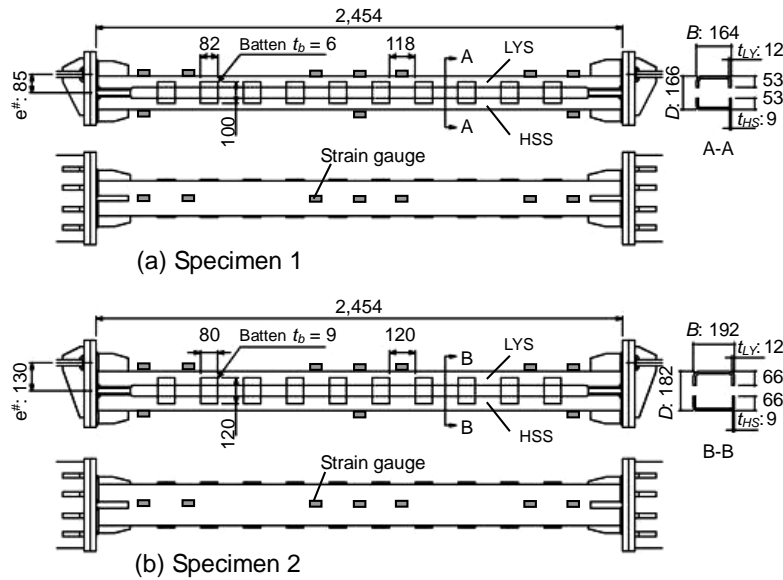| Specimen	Cross-section			High-strength steel (HS)				Low-yield-point steel (LY)			
	B	D	$e"$	t_{HS}	$\sigma_{y,HS}$	$\sigma_{u,HS}$	ε_{HS}	t_{LY}	$\sigma_{y,LY}$	$\sigma_{u,LY}$	ε_{LY}
	(mm)	(mm)	(mm)	(mm)	(MPa)	(MPa)	(%)	(mm)	(MPa)	(MPa)	(%)
Specimen 1	164	166	78.7	9.13	638	690	13.4	12.07	231	308	47.2
Specimen 2	192	182	121.8								
HLS-D20-E60	84	104	60.0	5.93	548	619	21.7	5.98	59	239	51.5

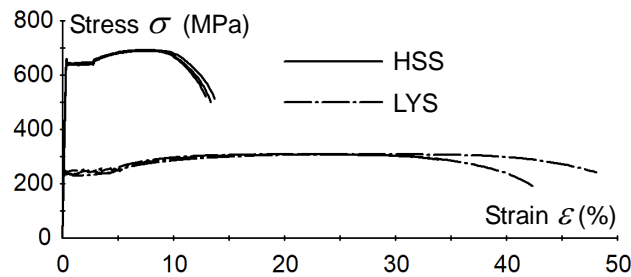**Fig. 3.** Tested Full-scale NBB specimens (dimensions in mm)

Fig. 4. Tensile coupon test results of HSS and LYS

In this paper, the NBB specimens have asymmetrical sections about x-axis because the LYS channel is thicker than the HSS channel. As a result, the center of gravity of the built-up section does not coincide with the member centerline. Fig. 5 illustrate the details of NBB-ends and the proposed end-plate gusset-plate connection. In Specimen 1, the eccentricity measured from the center line of the brace to the line of action of the force (defined as $e^{\#}$) is equal to 85mm. The actual intentional eccentricity determined based on the center of gravity, $e"$, is equal to 78.7mm because the center of gravity has been moved towards the LYS channel by 6.3mm. The intentional eccentricity of both specimens normalized by the corresponding radius of gyration, $e"/r_{com,}$ are equal to 1.23 for Specimen 1 and 1.63 for Specimen 2. Note that this ratio $e"/r_{com}$ for the reference specimen HLS-D20-E60 in Ref. [15] is equal to 1.42 which is larger than the corresponding ratio of Specimen 1. This is because $e"$ is smaller than the $e^{\#}$ when a thicker LYS channel is adopted.
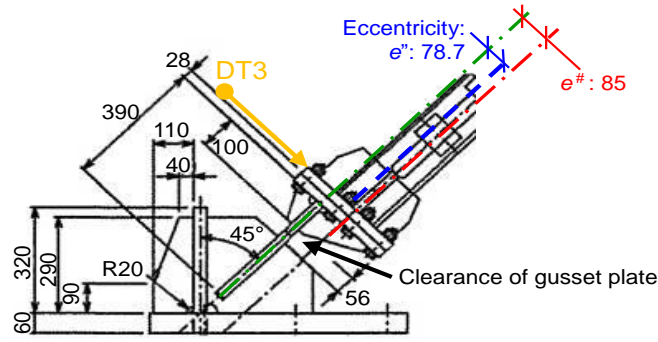
Fig. 5. Proposed in-plane gusset-plate connection of Specimen 1 (dimensions in mm)

3.2. Gusset-plate connection configuration for in-plane brace buckling

In NBB configuration, an appreciable improvement of the energy dissipation capacity has been proved by introducing the intentional eccentricity. The NBB tends to deform in the frame plane in which the intentional eccentricity is introduced. The authors have suggested a new simple pin-support configuration for NBB-ends using gusset plates [17]. These typical gusset-plate connections are designed to accommodate out-of-plane brace deformations. In this paper, an alternative connection that accommodates in-plane member buckling is proposed as in Ref. [19]. In-plane buckling results in reduced strain demands at brace ends [23]. Moreover, braces that would typically buckle in plane permit the construction of partition walls close to them. Fig. 5 illustrates the in-plane gusset-plate connection. The gusset plate is designed based on the AISC design specifications [34, 35]. A clearance distance twice the gusset plate thickness, t_p, (56mm) is considered. Assuming that a pin is formed at the middle of clearance distance, the pin-to-pin length of NBB, L is equal to 2,825mm. Thus, the member slenderness λ about x axis (see Fig. 1) is equal to $\lambda_x = 44.0$ and 37.9 for Specimen 1 and 2, respectively.

3.3. Loading protocol and measurement system

The loading frame system is shown in Fig. 6. NBB specimens are installed into the loading frame through the in-plane gusset-plate connections. The loading system is a four-pinned loading frame, therefore only the installed specimen resists the applied lateral load.
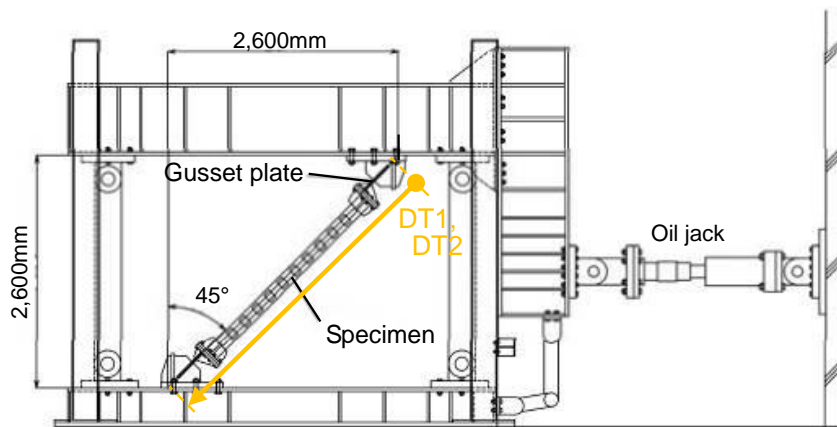

Fig. 6. Loading frame and measurement system (dimensions in mm)

The loading protocol consists of two symmetric cycles laterally imposed at each load amplitude of 0.25, 0.5, 0.75, 1.0, 1.5, and 2.0% SDR except for the SDR at which local buckling occurs in compression. At this SDR, loading cycles are repeated five times instead of two times to evaluate the

post-local bucking behaviour of the brace to cumulative damage. In Specimen 1, local buckling initiated during 1.5% SDR, while in Specimen 2, local buckling initiated during 2.0% SDR. Therefore, these SDRs were repeated five times for each specimen. In the previous experiments of NBB [15-17], a strength deterioration of the member was observed due to the onset of local buckling in LYS channel. In this research study, assuming that NBB is designed against a maximum SDR of 2%, the impact of cyclic deformation after local buckling on the ultimate performance is investigated. It should be noted that SDR is defined as the lateral displacement divided by the frame height (i.e., 2600mm) with the lateral displacement being the horizontal component of the brace axial displacement.

Fig. 6 also depicts the measurement system. Two displacement transducers (DT1 and DT2) to measure the axial displacement of the bracing member and one displacement transducer (DT3) to measure the in-plane rotation of the gusset plates are placed. Moreover, seven and three strain gauges are attached on the LYS and HSS channels, respectively, to detect yielding initiation, as shown in Fig. 3.

3.4. Test results

Fig.7 shows the axial load – axial displacement relationship of both specimens (solid line) compared to the backbone curve calculated based on the analytical relationships introduced in Section 2.2 (dotted line of Fig. 2). In both specimens, a high energy dissipation capacity without any strength deterioration was observed until an axial displacement of 27.6 mm (i.e., 1.5% SDR). For an axial displacement of 36.7mm (i.e., 2.0% SDR), strength deterioration was observed due to the onset of local buckling. The backbone curve appears to estimate the main elastic and inelastic quantities of brace response (i.e., elastic stiffness, compressive and tensile strength, post-yielding stiffness) with fairly good accuracy.

Fig. 8 depicts the overall deformation of brace specimens for an axial displacement of 27.6 mm (i.e., 1.5% SDR) under the 2nd compression cycle. Both specimens deformed in-plane of the frame and no excessive concentration of local deformation was observed. For each specimen, the cyclic behaviour as well as the ultimate performance are described in detail in the following paragraphs.
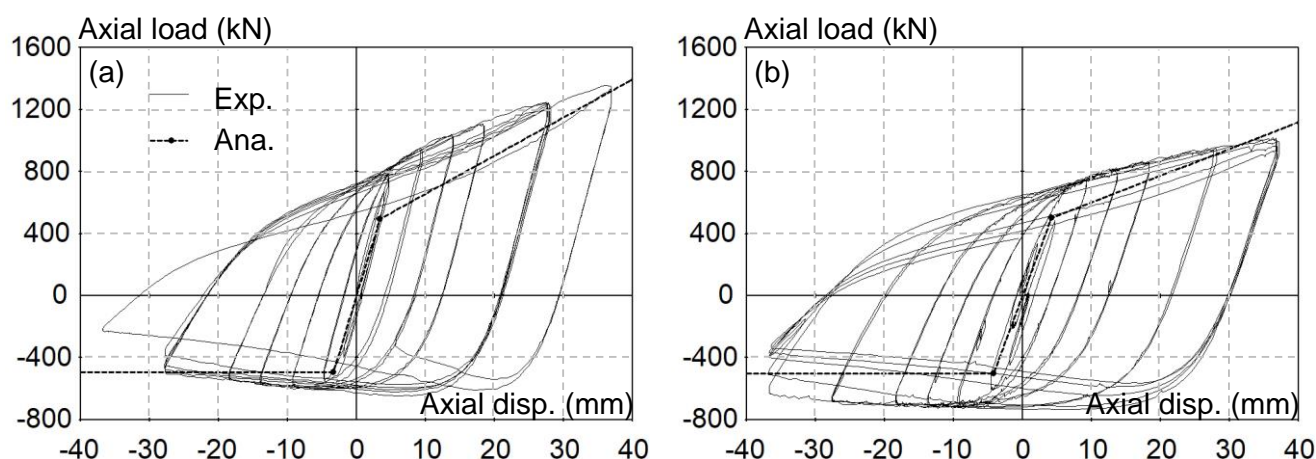
Fig. 7. Axial load – axial displacement relation; (a) Specimen 1, (b) Specimen 2
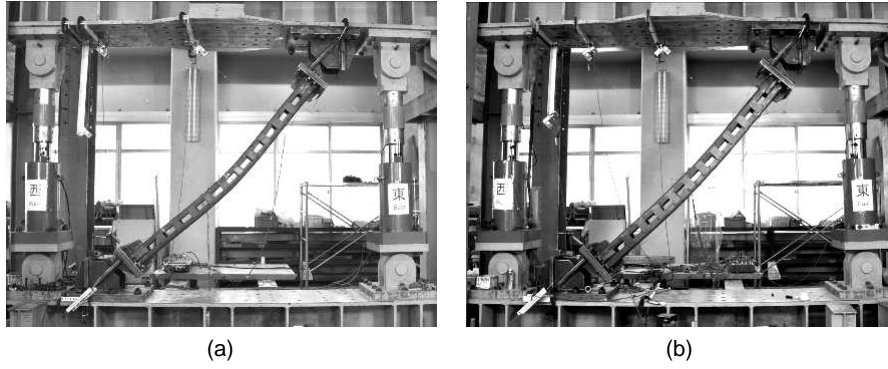
(a)   (b)

Fig. 8. Deformed shape of NBB specimens observed at a 1.5% SDR; (a) Specimen 1, (b) Specimen 2
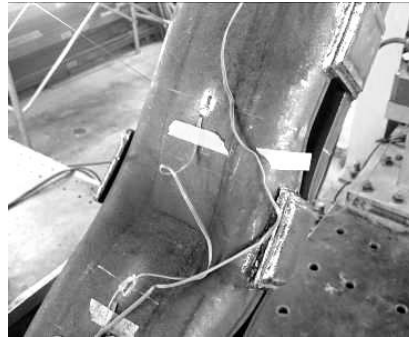

Fig. 9. Ultimate failure state of Specimen 1: buckling in the mid-length at LYS channel and welding failure of channel battens
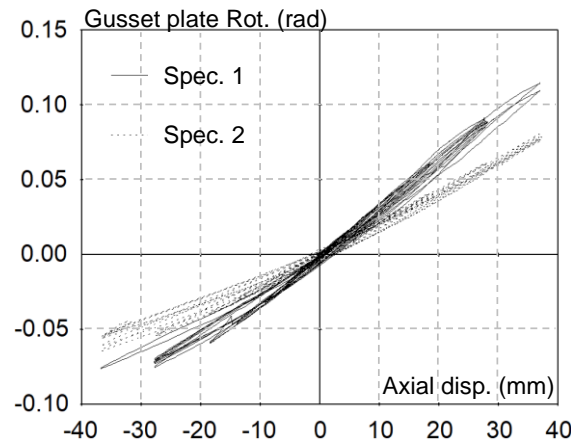

Fig. 10. Axial displacement –in-plane rotation relationship of gusset plates

Specimen 1 (this specimen has smaller eccentricity than Specimen 2) began to dissipate energy for an axial displacement of 3.8mm (i.e., 0.21% SDR). The LYS channel was yielded first as detected by the attached strain gauges. For an axial displacement of 4.6mm (i.e., 0.25% SDR), the specimen entered into the inelastic region of the tensile post-yielding stiffness while in compression, the specimen reached its maximum strength. Until the specimen reaches an axial displacement of 18.4mm (i.e., 1.0% SDR), the amount of energy dissipation was about the same under each loading cycle and the hysteresis loop was stable. For an axial displacement of 27.6mm (i.e., 1.5% SDR), a slight local buckling was observed at the mid-length of the LYS channel under the first loading cycle. At this amplitude, the loading cycles were repeated five times. In tension, no deterioration was observed during this repetitive loading. In compression, a slight strength deterioration was observed up to the 4th repeated loading cycle. Although

local buckling was more intense during the following 5th repeated cycle, the compressive strength maintained 79% of the strength that recorded in the 1st compressive cycle of this repeated loading. For an axial displacement of 36.7 mm (i.e., 2.0% SDR), local buckling increased and the compressive strength started to deteriorate but the tensile strength was further increased. During the 2nd cycle of the 2.0% SDR, the fillet welding around the steel battens was failed and battens were detached from the LYS channel during the compressive loading. Fig. 9 shows the failure of the batten region as well as the local buckling growth near the mid-length of the LYS channel at the end of the loading. In the reference specimen HLS-D20-E60 (half-scale specimen) [15], local buckling was observed at a 3.0% SDR which is a higher SDR than that observed in the full-scale Specimen 1 of this study. This might be attributed to the size effect as well as the fact that plastic strain localization in LYS channel of Specimen 1 was more severe. The latter is related to the smaller e''/r_{com} of Specimen 1 than that of the reference specimen HLS-D20-E60.

Specimen 2 (this specimen has larger eccentricity than Specimen 1) began to dissipate energy at an axial displacement of 4.0mm (i.e., 0.22% SDR). As shown in the axial load – axial displacement relationship (Fig. 8b), the specimen entered into the inelastic region of the tensile post-yielding stiffness and the compressive strength reached its maximum value under an axial displacement of 4.6mm (i.e., 0.25% SDR). Until the specimen reached an axial displacement of 27.6mm (i.e., 1.5% SDR), the specimen exhibited a stable hysteretic behaviour and no difference was observed in the amount of dissipated energy in each cycle. For an axial displacement of 36.7mm (i.e., 2.0% SDR), local buckling was observed in the LYS channel, therefore, this cycle was repeated five times to evaluate the growth of local buckling. Since the Specimen 2 has larger section and eccentricity than Specimen 1, this enhances the plastic deformation capacity of the member and the SDR at which local buckling occurred was found to be higher. Under the five repeated loading cycles of 36.7mm axial displacement, the compressive strength was reduced more in compression than in tension. This behaviour is likely to be related to the high elasticity of the HSS channel and the large isotropic hardening of the LYS channel. The compressive strength during the 5th repeated cycle decreased to 53.4% of the strength recorded in the 1st compressive cycle of the repeated loading cycles. On the contrary, the strength in tension maintained 92.4% of the tensile strength recorded in the 1st tensile loading cycle of the repeated loading. Similarly, with Specimen 1, the SDR at which local buckling occurred in Specimen 2 is smaller than the one observed in the reference specimen HLS-D20-E60 (i.e., 3.0% story drift) even if e''/r_{com} of Specimen 2 is larger than that of HLS-D20-E60 (i.e., 1.63 and 1.42, respectively). Nonetheless, referring to the channel width-to-thickness ratio B/t_{LY}, this is 14.0 for the HLS-D20-E60 and 15.9 for the Specimen 2 (i.e., 14% larger) which makes the inelastic response more prone to size effect. In Specimen 2, although the level of plastic strain localization is less severe compared to HLS-D20-E60 due to the larger e''/r_{com}, the difference in width-to-thickness ratio B/t_{LY} appears to have a stronger influence on local buckling.

Fig. 10 shows the relationship between the brace axial displacement and the gusset plate in-plane rotation as obtained from both Specimen 1 and Specimen 2. The rotation of the gusset-plate connection is based on the displacements measured from the displacement transducer DT3 (Fig. 6) divided by 142mm which is the distance from DT3 to the center of the clearance distance of the gusset plate. In both specimens, this relation was found to be almost linear. The maximum measured rotation was 0.12 rad for Specimen 1 and 0.08 rad for Specimen 2. Neither fracture nor cracks were observed in the gusset-plate connections. These measured rotation values are very similar with those of other tests where out-of-plane pinned gusset-plate connections or mechanical pins were used [17, 19, 37]. This indicates that the proposed in-plane gusset-plate connections behaved well and can successfully accommodate the required rotation demands of NBB deformation.

4. Finite Element Modeling of NBB and parametric study

In this section, a computational study of the cyclic behaviour of the NBB specimens was performed using the finite element (FE) simulation software ABAQUS [38]. To verify the reliability of the proposed detailed FE model, the computational simulation results were compared with the experimental results. The loading pattern followed for the finite element analysis is the same as the one used in experiments.

4.1. Finite Element Model

Fig. 11 illustrates the FE model of an NBB. An HSS channel section with 9 mm thickness and a LYS channel section with 12 mm thickness are adopted for the brace configuration (Fig. 11a). The model was divided into 30 elements along the steel section and more than 100 elements along the length for each section (Fig. 11b). Fine rectangular mesh along with linear quadrilateral 4-noded S4R shell elements of reduced integration were used for the FE analysis. A material with a yield strength of 638 MPa was assigned in each fiber of HSS section and a material with a yield strength of 231 MPa was assigned in each fiber of LYS section. For LYS, where isotropic hardening is significant [39], isotropic hardening in addition to kinematic hardening was combined in the material property, whereas for the HSS, only kinematic hardening was applied. HSS and LYS sections were connected together by providing battens along the brace length. Tie constraint was used to define the contact between battens and channel section surfaces. Both ends of the brace were provided with gusset plates having a $2t_p$ clearance distance to act as pinned connections at an eccentricity specified in Section 3.2 for each specimen. A multi-point constraint (MPC) was used to connect the gusset plates and the brace member. An incremental displacement-controlled analysis was performed to one brace end for simulation. The brace was arranged in the same angle as in the experiment.
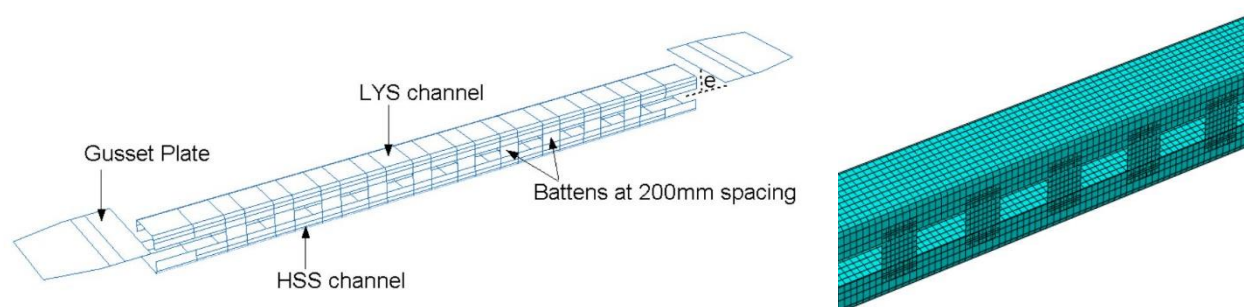

Fig. 11. Finite element modeling: (a) entire FE model with gusset plates; (b) Meshed view of channels and battens

The properties of specimens used for the computational study are summarized in Table 2. In this study, Specimen 1 is denoted as SP1 and Specimen 2 as SP2. The comparison of results from experimental and FE analysis studies are shown in Fig. 12 and Fig. 13. From both figures, one can observe that the FE model can simulate the test with a good accuracy. The full details of the gusset-plate connections were not modelled as a choice to reduce the computational time and complexity of the model. In both specimens, the finite element model meticulously captured local buckling at 2% SDR, same as observed in the experiment and as discussed in Section 3.4. The deterioration in compressive strength at this point can also be observed from the results. In SP1, the local buckling was induced during the 1st compression cycle of 1.5% SDR and became evident at a 2% SDR. The sudden drop in strength under compression can also be observed from the FE hysteretic loop similar to test results. In case of SP2, which has larger section and eccentricity compared to Specimen 1, the local buckling was induced during the 1st compression cycle of 2% SDR and a strength decrease in compression was observed for this specimen,
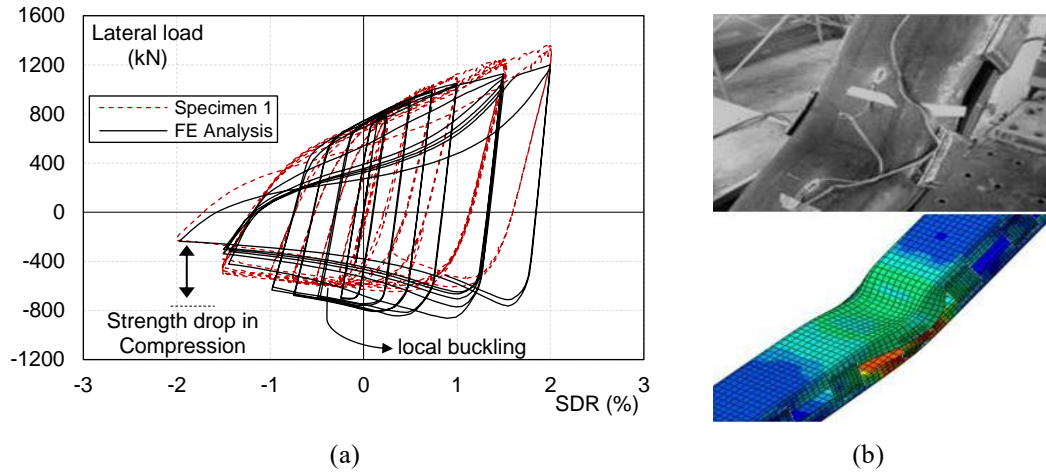
417 too.

418 **Table 2** Properties of different specimens used for numerical simulation.

SPECIMEN	L	$e^{\#}$	t_{LY}	t_{HS}	$\sigma_{y,LY}$	$\sigma_{y,HS}$	t_Batten	$t\_Stiffener$	$Stiffener$ $No.$ (n)
	(mm)	(mm)	(mm)	(mm)	(MPa)	(MPa)	(mm)	(mm)	
SP1	2825	85	12	9	231	638	6	0	0
SP2	2825	130	12	9	231	638	9	0	0

419

420

(a)   (b)

423 **Fig.12.** Test results compared with FE analysis results for Specimen 1: (a) Lateral load - SDR relation; (b) Deformed
424 shape at the mid-length of the LYS channel

425

(a)   (b)
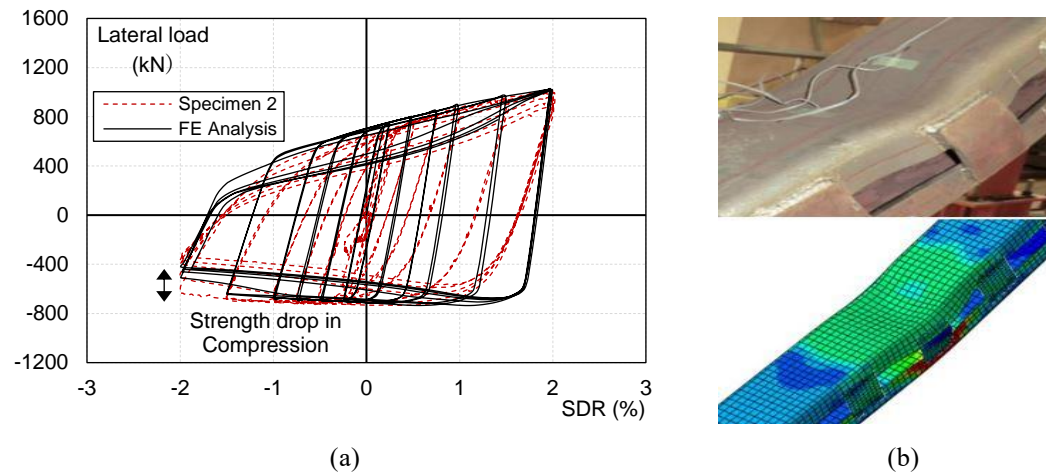
428 **Fig.13.** Test results compared with FE analysis results for Specimen 2: (a) Lateral load - SDR relation; (b) Deformed
429 shape at the mid-length of the LYS channel

430 *4.2. Parametric study and performance evaluation indices*

431   As local buckling was observed in LYS channel of NBB during the experimental study, strengthening
432 of NBB by utilizing stiffeners in the critical zones or by increasing the thickness of battens is explored.
433 The use of stiffeners appears to be a straightforward strengthening approach as NBB consists of open
434 channel sections. The stiffeners combined with the eccentricity that is introduced along the brace length
435 can more evenly distribute the local stresses in the middle area, thereby the onset of local buckling could

be further delayed. This can also prevent the brace from undesirable local buckling related failures, such as the sudden welding failure of channel battens seen in these tests (Fig. 9). In this section, a parametric study was conducted to understand the effect of stiffeners and thickness of battens on the performance of NBB and to evaluate their efficiency in strengthening of NBB against local buckling. For that purpose, models with stiffeners were developed in ABAQUS as shown in Fig. 14. Rib stiffeners were placed exactly in the position of the battens and in the clearance distance between them. The rib stiffeners were placed along the central part of the brace. The parametric study considered the effect of the number and thickness of stiffeners as well as the thickness of battens.
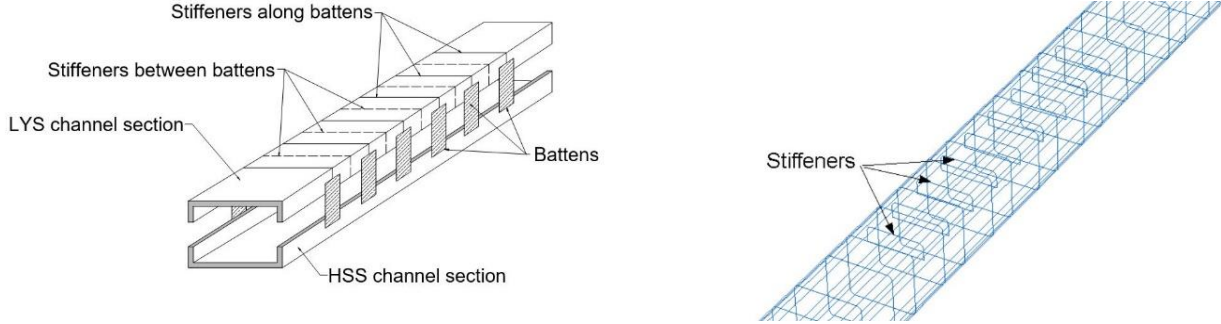

Fig. 14. FE model with rib-stiffened section for the parametric study

Using the hysteretic curves of each analysis model, the normalized dissipated energy is calculated to evaluate the hysteretic behaviour and energy dissipation capacity of braces [40]. On the basis of this index, one can evaluate the influence local buckling has on the cyclic response and how the progress of local bucking affects the dissipative capacity of the member. More specifically, a comparison is made according to the equivalent viscous damping ratio, ξ_{eq}, by adopting the relation [41]:

$$\xi_{eq} = \frac{E_d}{2\pi F_m \Delta_m} \tag{10}$$

where E_d is the energy dissipation in a given complete cycle of the force-displacement curve; F_m is the maximum force in a given cycle and Δ_m is the corresponding displacement. The results are calculated considering a symmetrical hysteretic F-Δ relation as obtained for chevron brace configurations (i.e., both compression and tension cycles are considered). It should be noted that ξ_{eq} accounts for the energy dissipation by nonlinear F-Δ relations as expected during strong earthquakes.

Moreover, the magnitude of plastic strain (PEMAG) and equivalent plastic strain (PEEQ) curves are prepared for each specimen set as additional performance evaluation indices to ξ_{eq}, in order to identify the best brace configuration in terms of ductility capacity. PEEQ is defined as $\int_0^t \dot{\bar{\varepsilon}}^{pl} dt$ where for classical metal (Mises) plasticity $\dot{\bar{\varepsilon}}^{pl} = \sqrt{2/3\dot{\varepsilon}^{pl} : \dot{\varepsilon}^{pl}}$ and $\dot{\varepsilon}^{pl}$ is the plastic strain rate. Both PEMAG and PEEQ are scalar measures of the accumulated plastic strain. For proportional loading, the measures should be equal. However, for loading with reversals like cyclic loading, PEEQ will continue to increase if the plastic strain rate is non-zero (regardless of sign) and is an important index to evaluate the cumulative damage of a structural member. These quantities provide a measure of the strain in the specimen. Higher the plastic strain, lower will be the ductility performance of the model. Effect of each parameter is discussed in the following sections.

4.2.1. Effect of number of stiffeners on Specimen 1

In order to evaluate the effect of numbers of stiffening ribs on NBB's cyclic performance, six NBB models with different numbers of stiffening ribs were developed on the basis of design details of test Specimen 1. The model properties are shown in Table 3. Nomenclature of the specimens used for the study follows the order, SP1-nSTt_Stiffener-Bt_Batten where SP1 represents Specimen 1 and SP2 stands for Specimen 2. ST represents the stiffeners and B represent the battens. Letter 'n' denotes the number of stiffeners used, t_Stiffener shows the thickness of stiffeners and t_Batten denotes the thickness of battens. The six models maintained their size, eccentricity, stiffening rib and batten thickness factors identical except for the number of stiffening ribs. Fig. 15a-f shows the different specimen categories along with their stiffener position and numbers. The ξ_{eq} curves, and PEMAG and PEEQ curves of the six models are shown in Fig. 16. PEMAG always refers to the brace ends (i.e., LYS channel) subject to both bending and axial loads, while PEEQ in areas prone to local buckling (i.e., usually in the middle length of the brace). In addition, Fig. 16c plots the threshold for PEEQ (≈ 0.58). This value corresponds to the PEEQ at which local buckling occurred in FE simulations of Specimen 1 (Fig. 12: 1st compression cycle of 1.5% SDR). It should be noted that ξ_{eq} was computed considering the complete cycles of the response at each amplitude (i.e., compression and tension). In Figs. 16b and c, the horizontal axis refers to the 2nd tensile loading cycle of each SDR of the low-cycle fatigue protocol considered in this study.

Table 3 Properties of SP1 specimens with varying number of stiffening ribs.

SPECIMEN	L (mm)	$e^{\#}$ (mm)	t_{LY} (mm)	t_{HS} (mm)	$\sigma_{y,LY}$ (MPa)	$\sigma_{y,HS}$ (MPa)	t_Batten (mm)	$t\_Stiffener$ (mm)	Stiffener No. (n)
SP1	2825	85	12	9	231	638	6	0	0
SP1-1ST9-B6	2825	85	12	9	231	638	6	9	1
SP1-3ST9-B6	2825	85	12	9	231	638	6	9	3
SP1-5ST9-B6	2825	85	12	9	231	638	6	9	5
SP1-7ST9-B6	2825	85	12	9	231	638	6	9	7
SP1-9ST9-B6	2825	85	12	9	231	638	6	9	9
SP1-12ST9-B6	2825	85	12	9	231	638	6	9	12

(a) SP1-1ST9-B6

(b) SP1-3ST9-B6

(e) SP1-5ST9-B6

(c) SP1-7ST9-B6

(d) SP1-9ST9-B6

(f) SP1-12ST9-B6
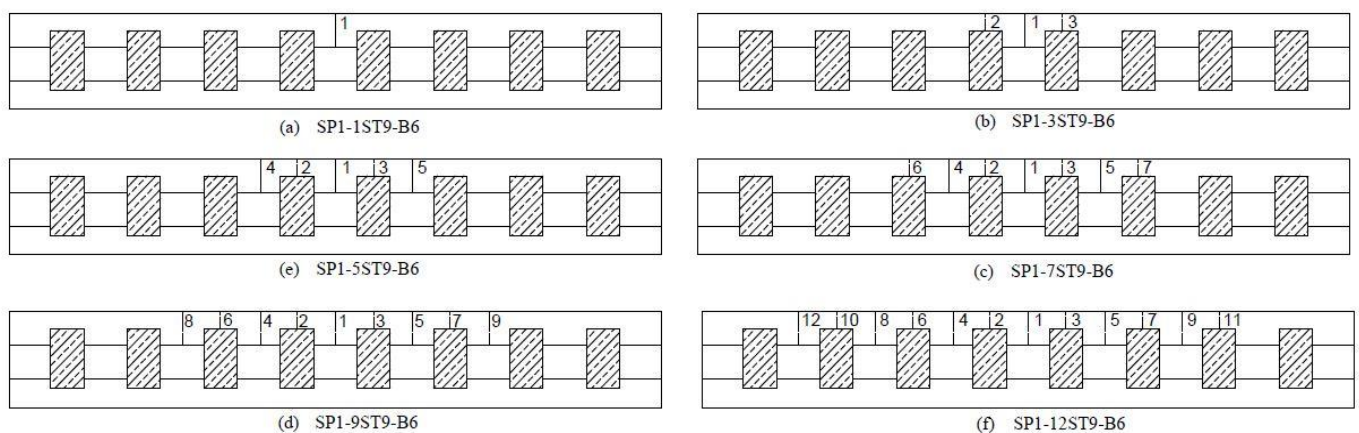
Fig.15. Specimen categories with varying specimen numbers
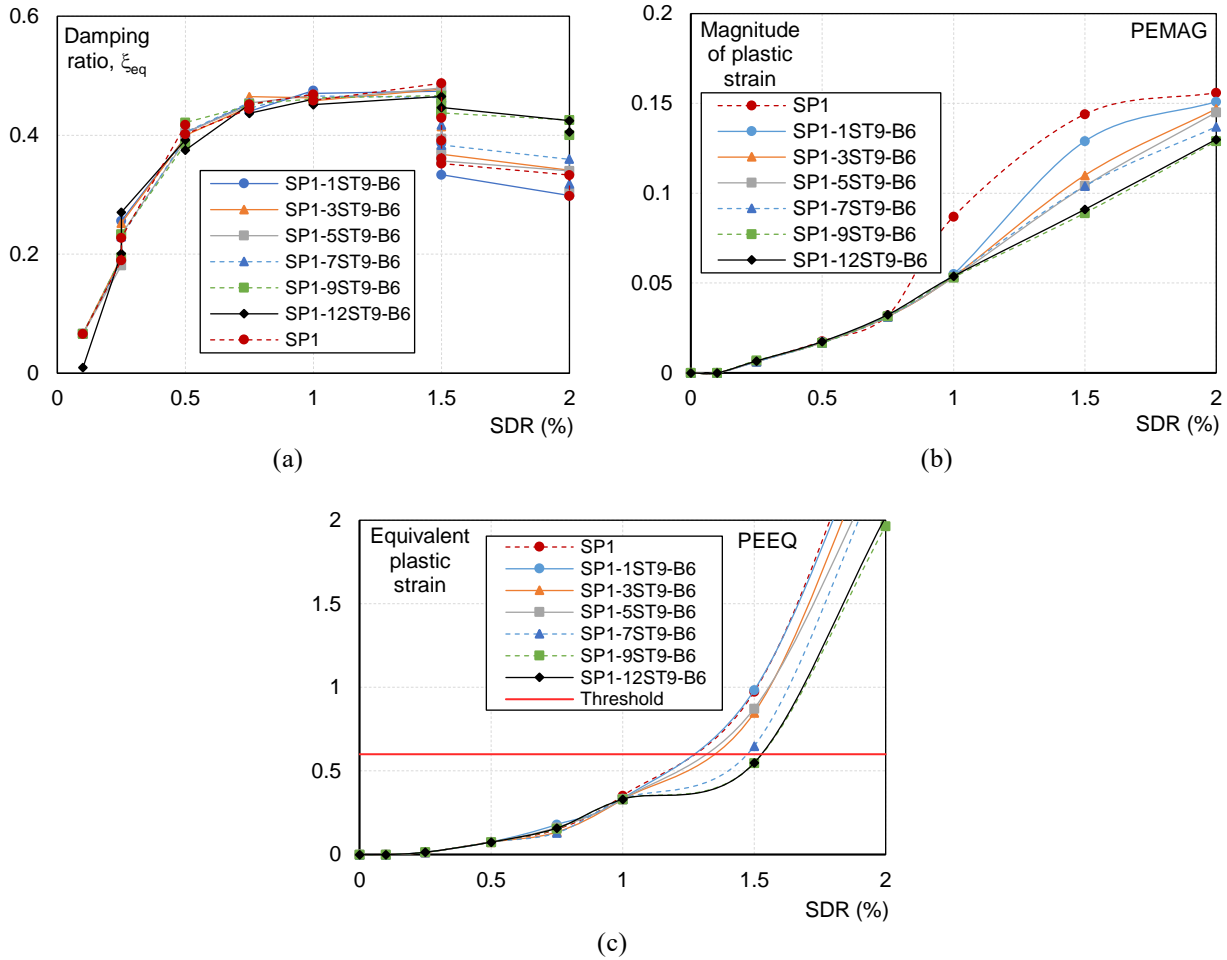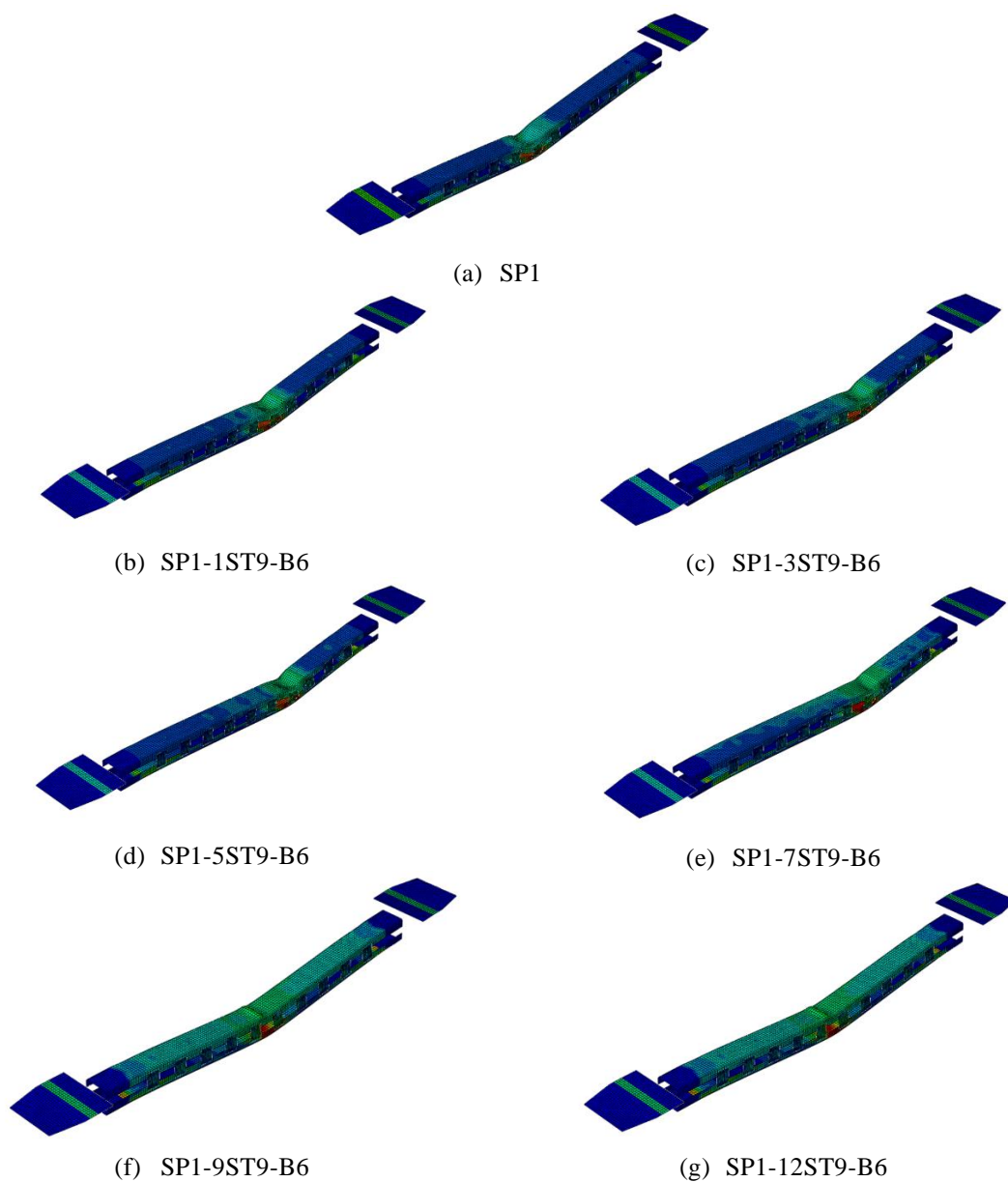
(a)

(b)

(c)

Fig. 16. Relation of SDR with: (a) Equivalent damping ratio; (b) Magnitude of plastic strain (PEMAG); (c) Equivalent plastic strain (PEEQ), for the FE models under the influence of varying stiffener number.

SP1 with stiffeners has the potential to present a 35% increase in its damping ratio at 2% SDR compared to SP1 without stiffeners (Fig. 16a). This demonstrated the fact that stiffeners increase the energy dissipating capacity of the brace considerably thereby strengthening its behaviour against local buckling. As shown in Fig. 16a, with the increase of the number of stiffening ribs in the model, its equivalent damping ratio value also increases but its noteworthy that, when the number of stiffening ribs increases to 9 (SP1-9ST9-B6), the curve tends to be stable. When the number of stiffening ribs increases to 12, i.e., when the model is almost filled with stiffening ribs (SP1-12ST9-B6), the equivalent damping ratio curve at this point almost matches the curve of the model with the 9 stiffening ribs, indicating no further improvement.

The PEMAG and PEEQ values were obtained from FE analysis results for the various SDR levels. In the PEMAG curve (Fig. 16b), the curve with the smallest strain corresponds to the models with 9 stiffening ribs (SP1-9ST9-B6) and 12 stiffening ribs (SP1-12ST9-B6), thereby, making the former the ideal configurations for this specimen. In the effective strain curve of PEEQ (Fig. 16c), both SP1-9ST9-B6 and SP1-12ST9-B6 exhibit the lowest PEEQ value at 2% SDR. Moreover, for 1.5% SDR, PEEQ is lower than the threshold for both models indicating that local buckling failure is likely to be restrained during the repeated compression cycles of 1.5% SDR. More specifically, based on the FE analysis, a very slight local buckling occurred during the 3rd compression cycle of 1.5% SDR. Thus, 9 stiffening ribs appear to be adequate for Specimen 1. It should be noted, that once local buckling occurs, plastic strain accumulation takes place in the vicinity of damaged area resulting in very high values of PEEQ. The values tend to rapidly increase with the repeated loading cycles, as shown in Fig. 16c.

Fig. 17 depicts the overall deformation of all FE models listed in Table 3 for the 5th compression loading cycle of 1.5% SDR. By observing this figure, one can see that there is a considerable improvement in the performance of the model in terms of restraining mid-length local buckling by increasing the number of stiffeners to 9 (Fig. 17a-g). The model with 12 stiffeners shows the same overall performance with the model of 9 stiffeners (Fig. 17f-g). This observation can be attributed to the fact that 9 stiffeners themselves are enough to strengthen the central part of this NBB specimen there by strengthening it to maximum extent and creating no difference even if greater number of stiffeners are accommodated. This is in accordance with the finding of Fig. 16. In general, it can be stated that NBBs can be strengthened by applying stiffeners in two-thirds of its total length along the central part leaving both brace ends unstiffened. Further investigation is required to validate this finding considering as a parameter the slenderness of the brace. Finally, when less than 9 stiffeners are used (Fig. 17b-e), an unsymmetrical buckling behaviour was observed as the plastic hinge is formed within the unstiffened brace length. A similar observation has been made in Ref. [23] where partial material strengthening was introduced for a certain length of the brace.

(a) SP1

(b) SP1-1ST9-B6

(c) SP1-3ST9-B6

(d) SP1-5ST9-B6

(e) SP1-7ST9-B6

(f) SP1-9ST9-B6

(g) SP1-12ST9-B6

**Fig.17.** Overall deformation of all FE models listed in Table 3 for the 5th compression loading cycle of 1.5% SDR

4.2.2. Effect of stiffener thickness on Specimen 1

To evaluate the effect of different thicknesses of stiffening ribs on NBB performance, four models with the same size, eccentricity, number of stiffening ribs, and batten thickness were created, varying the thickness of stiffening ribs to 6 mm, 9 mm, 12 mm and 15 mm for comparison. The properties of the four models are summarized in Table 4. The ξ_{eq} curves, and PEMAG and PEEQ curves of the three models are shown in Fig. 18 in the same manner with Fig. 16.

Table 4 Properties of specimens with varying stiffener thickness.

SPECIMEN	L (mm)	$e^{\#}$ (mm)	t_{LY} (mm)	t_{HS} (mm)	$\sigma_{y,LY}$ (MPa)	$\sigma_{y,HS}$ (MPa)	t_Batten (mm)	t_Stiffener (mm)	Stiffener No. (n)
SP1-9ST6-B6	2825	85	12	9	231	638	6	6	9
SP1-9ST9-B6	2825	85	12	9	231	638	6	9	9
SP1-9ST12-B6	2825	85	12	9	231	638	6	12	9
SP1-9ST15-B6	2825	85	12	9	231	638	6	15	9

(a)

(b)

(c)
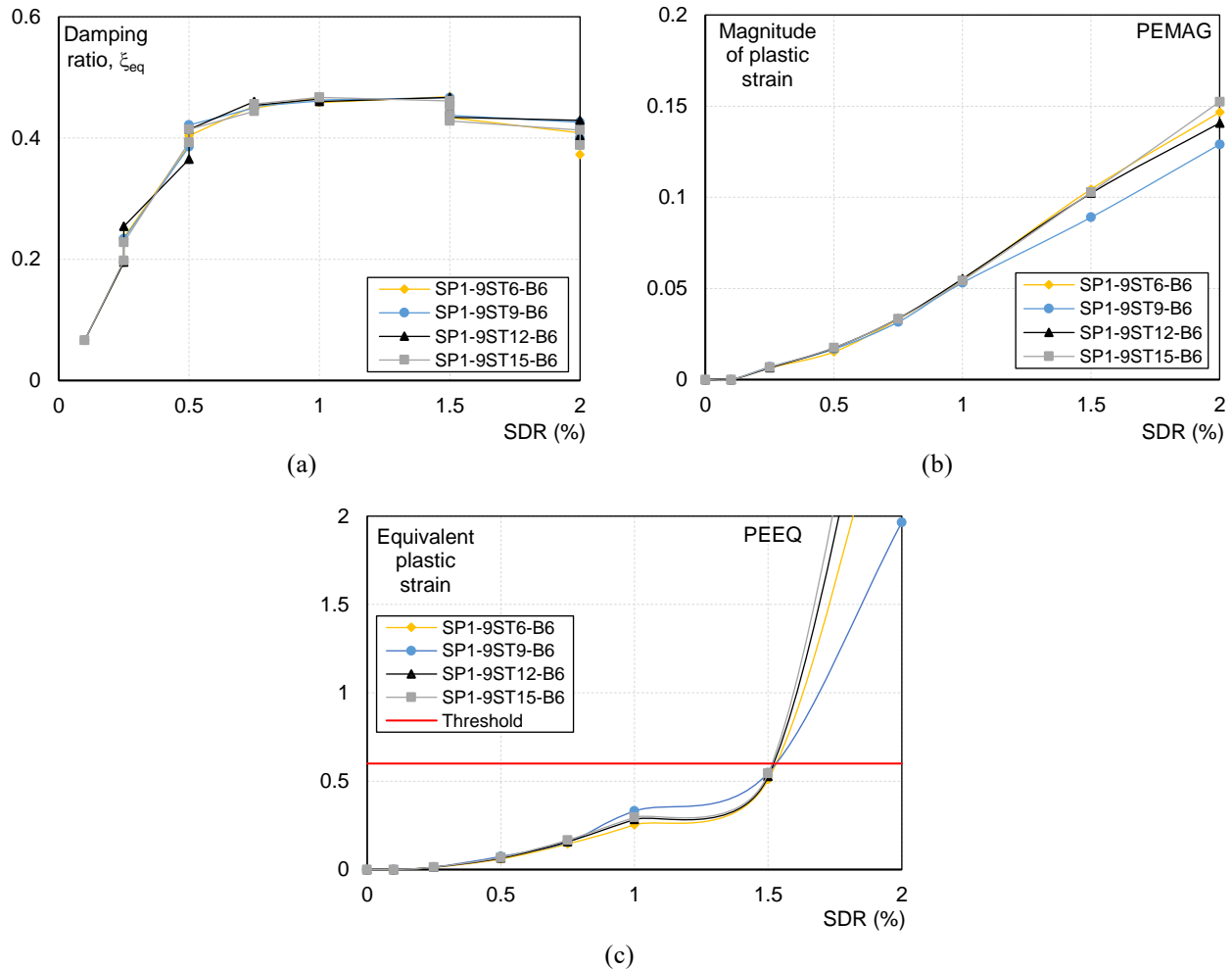
Fig. 18. Relation of SDR with: (a) Equivalent damping ratio; (b) Magnitude of plastic strain (PEMAG); (c) Equivalent plastic strain (PEEQ), for the FE models under the influence of varying stiffener thickness.

By observing Fig. 18a, the equivalent damping ratio for all FE models are not very different but takes the maximum value when the thickness of the rib stiffener is 12 mm (SP1-9ST12-B6). A very close

value is obtained when the thickness of the rib stiffener is 9 mm (SP1-9ST9-B6). On the contrary, the damping ratio is lowest when the rib thickness is 6 mm (SP1-9ST6-B6). By observing the PEMAG and PEEQ curves in Fig. 18b and c, respectively, the model SP1-9ST9-B6 exhibits the lowest strain values indicating a higher reserved ductility capacity to tension loads. Moreover, for 1.5% SDR, PEEQ is lower than the threshold for all cases indicating that local buckling is likely to be prevented during the compression cycles of 1.5% SDR. Among the specimens, SP1-9ST6-B6 exhibits the best post-local buckling behaviour in terms of plastic strain accumulation reaching the lower value after the completion of the five repeated cycles of 1.5% SDR and the two cycles of 2.0% SDR. Fig. 18c indicates that the thicker stiffeners are effective to restrain local buckling, but once local buckling occurs, they tend to increase plastic strain demands in the vicinity of damaged area more than the medium thickness ribs. As a result, 9mm-stiffeners were found to be most efficient in reducing local buckling of Specimen 1 which has a channel width-to-thickness ratio B/t_{LY} equal to 13.60.

### 4.2.3. Effect of batten thickness on Specimen 1

As a third parameter, the effect of batten thickness on NBB was studied. Three models with the same size and eccentricity but different batten thicknesses were modelled with batten thicknesses of 6 mm, 9 mm, and 12 mm. It is reminded here that in the corresponding Specimen 1 of the experimental campaign, the thickness of battens was equal to 6 mm. Here, the models considered has varying batten thickness but no stiffeners. This is to understand the effect of batten thickness alone without the influence of stiffeners. The use of thicker battens would be an alternative strengthening process to stiffening ribs. The properties of the three models are shown in Table 5. The ξ_{eq} curves, and PEMAG and equivalent PEEQ curves as obtained from the FEA are shown in Fig. 19a, b and c respectively, in the same manner with Fig. 16.

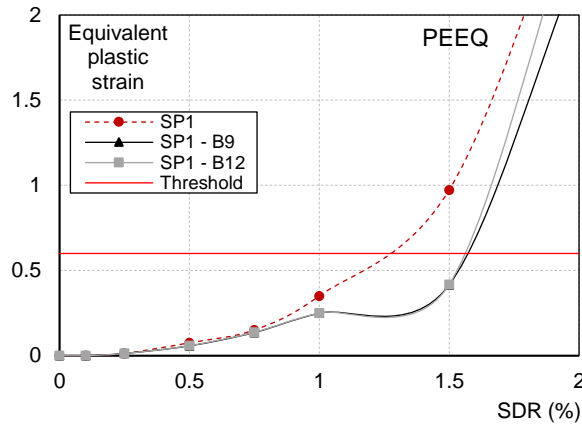**Table 5** Properties of specimens with varying batten thickness.

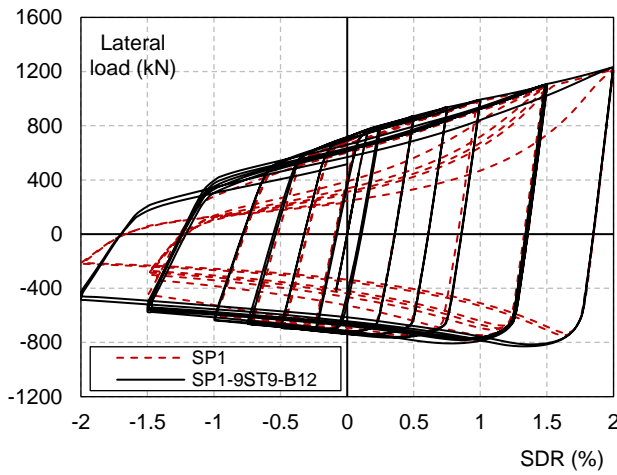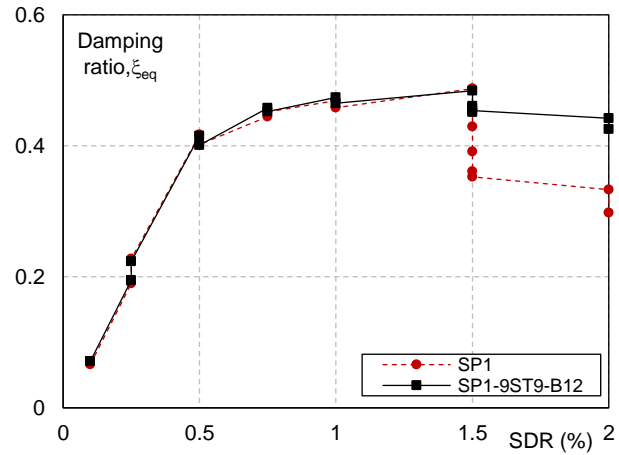| SPECIMEN	L (mm)	$e^{\#}$ (mm)	t_{LY} (mm)	t_{HS} (mm)	$\sigma_{y,LY}$ (MPa)	$\sigma_{y,HS}$ (MPa)	t_Batten (mm)	t_Stiffener (mm)	Stiffener No. (n)
SP1	2825	85	12	9	231	638	6	0	0
SP1 - B9	2825	85	12	9	231	638	9	0	0
SP1 - B12	2825	85	12	9	231	638	12	0	0
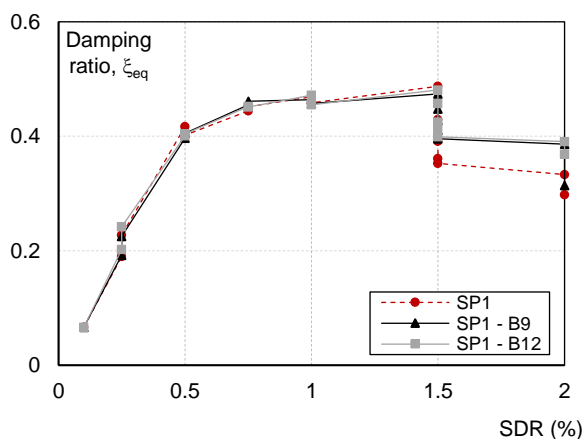
(a)
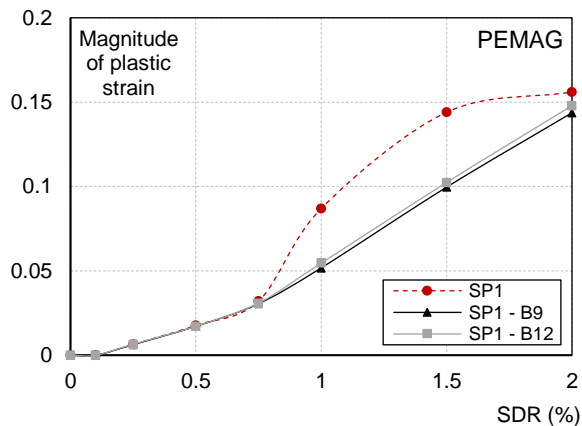
(b)

(c)

Fig. 19. Relation of SDR with: (a) Equivalent damping ratio; (b) Magnitude of plastic strain (PEMAG); (c) Equivalent plastic strain (PEEQ), for the FE models under the influence of varying batten thickness.

(a)

(b)

Fig. 20. Comparison between SP1 and SP1-9ST9-B12 analysis results: (a) Lateral load – SDR relationship; (b) Damping ratios – SDR relation.

The difference between the equivalent damping ratio curves of the group of models in Table 5 is small, and almost coincide for the two models with batten thicknesses of 9 mm (SP1-B9) and 12 mm (SP1-B12), respectively, as shown in Fig. 19a. For 2% SDR, the damping ratio of the model with 9 mm-battens is nearly 0.31, while that of the model with 12 mm-battens is higher and equals 0.37. This is because SP1–B9 exhibits greater strength degradation than SP1–B12 at this drift level. Observing the PEMAG and PEEQ curves in Fig. 19b and c, respectively, both models reach almost similar values at 1.5% SDR, indicating a similar damage at this drift level. Based on these observations, both battens appear to be effective, but SP1–B12 can be considered as the one with the more stable cyclic behaviour.

On the basis of the above parametric study related to Specimen 1, a better cyclic behaviour was observed in the FE model designed to have 9 stiffeners with 9 mm thickness and channel battens with 12 mm thickness. This model is denoted as SP1-9ST9-B12 and is compared with the non-strengthened FE model SP1 in Fig. 20a and b. Overall, a 43% increase was observed in its equivalent damping ratio compared to SP1 with no stiffeners at 2% SDR, while no sudden drop of compressive strength was observed until the very end of the damaging loading protocol. The use of sufficiently thick stiffeners and battens can strengthen NBB's energy dissipation capacity up to high inelastic levels, indicating that

NBB shall be used as a reliable damping system. Future experimental work is required to validate these findings.

4.2.4. Effect of stiffeners on Specimen 2

The effectiveness of stiffeners in SP2 is also investigated in this section. As SP2 has different section and eccentricity compared to SP1, a different combination of the number of stiffeners, thickness of stiffeners and thickness of battens were investigated for this case. The details of specimens used for this comparison are shown in Table 6. In SP2, rib stiffeners with 12 mm thickness were initially designed considering that SP2 has larger channel width-to-thickness ratio B/t_{LY} (i.e., 16.0) than SP1 (i.e., 13.6), thus more vulnerable to local buckling. The ξ_{eq} curves, and PEMAG and PEEQ curves as obtained from the FE analysis are shown in Fig. 21a, b and c, respectively. In addition, Fig. 21c plots the threshold for PEEQ (≈ 0.59). This value corresponds to the PEEQ at which local buckling occurred in FE simulations of Specimen 2 (Fig. 13: 1st compression cycle of 2.0% SDR). In Figs. 21b and c, the horizontal axis refers to the 2nd tensile loading cycle of each SDR of the loading protocol considered in this study.

SP2 with stiffeners exhibits a better performance in terms of its energy dissipation capacity compared to SP2 without stiffeners (Fig. 21a). There is almost 35% increase in its equivalent damping ratio at 2% SDR when stiffeners are applied along the central part of the brace. From the ξ_{eq} curves and PEMAG and PEEQ curves, the model SP2-9ST18-B18 and SP2-13ST18-B18 exhibit a similar performance.

**Table 6** Properties of SP2 with varying parameters.

SPECIMEN	L (mm)	$e^{\#}$ (mm)	t_{LY} (mm)	t_{HS} (mm)	$\sigma_{y,LY}$ (MPa)	$\sigma_{y,HS}$ (MPa)	t_Batten (mm)	$t\_Stiffener$ (mm)	*Stiffener No. (n)*
SP2	2825	130	12	9	231	638	9	0	0
SP2-9ST12-B6	2825	130	12	9	231	638	6	12	9
SP2-9ST12-B9	2825	130	12	9	231	638	9	12	9
SP2-9ST12-B12	2825	130	12	9	231	638	12	12	9
SP2-9ST12-B18	2825	130	12	9	231	638	18	12	9
SP2-9ST18-B18	2825	130	12	9	231	638	18	18	9
SP2-13ST18-B18	2825	130	12	9	231	638	18	18	13

(a)   (b)
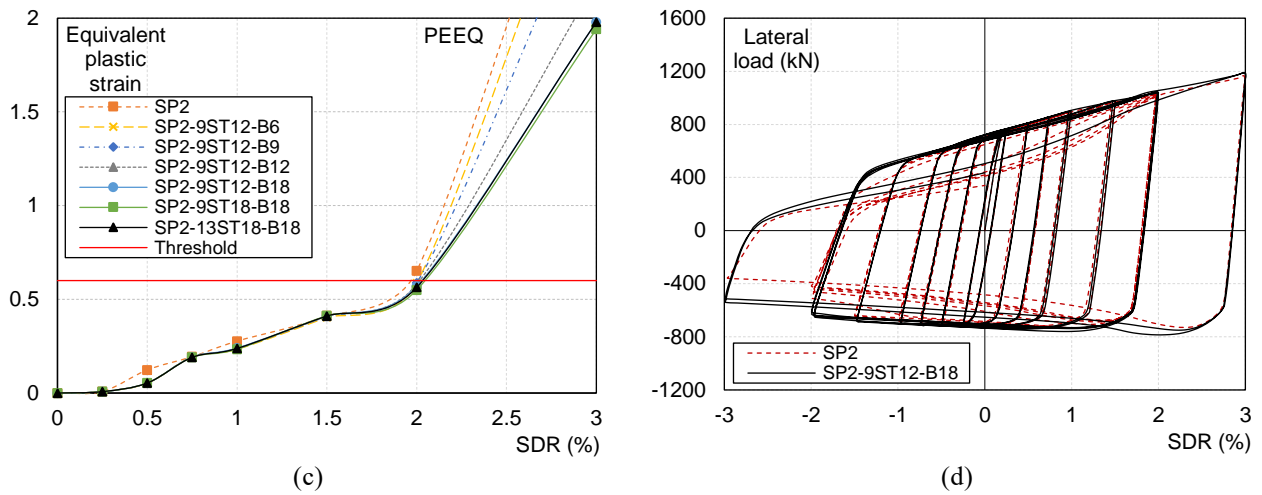
(c) (d)
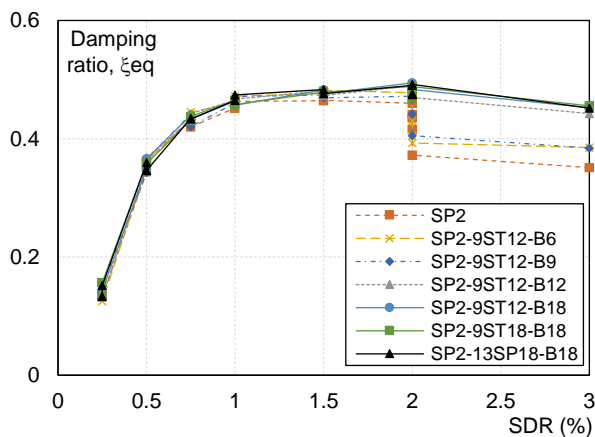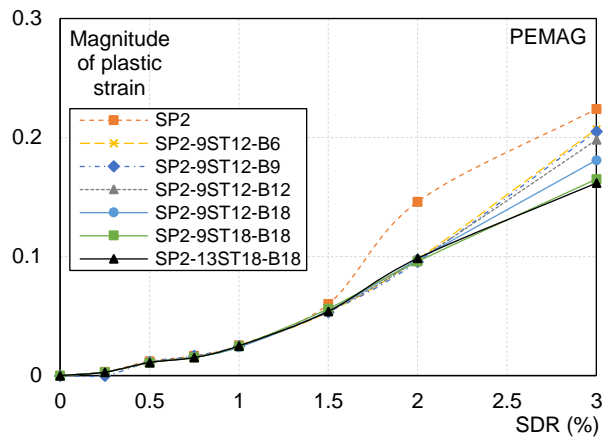
Fig. 21. Relation of SDR with: (a) Equivalent damping ratio; (b) Magnitude of plastic strain (PEMAG); (c) Equivalent plastic strain (PEEQ), for the FE models under consideration; (d) Comparisons of lateral load – SDR relation between SP2 and SP2-9ST12-B18.

In Figs. 21b and c, the model SP2-9ST18-B18 and model SP2-13ST18-B18 exhibited lowest strain values between 2% and 3% SDR compared to other models. When the stiffener number was increased to 13, the performance of the brace was similar to the model with 9 stiffeners resulting in the same number of stiffeners as in Specimen 1. The PEEQ values at 2% SDR hold below the threshold level for all strengthened NBB models. This indicates that the local buckling is successfully delayed. More specifically, a gentle local buckling was observed during the 4th compression cycle of 2% SDR for SP2-9ST18-B18 and SP2-13ST18-B18, while during the 3rd compression cycle of 2% SDR for the rest of the models. It is reminded here that in the corresponding Specimen 2 of the experimental campaign, the thickness of battens was equal to 9 mm. Based on Fig. 21a, the larger the thickness of battens, the more stable the hysteretic behaviour under the repeated loading cycles and the large inelastic deformations. Nevertheless, the FE model SP2-9ST12-B12 which has 9 stiffeners of 12 mm thickness and battens of 12 mm thickness, exhibits an equally good performance with SP2-9ST18-B18. The only difference is observed in the values of PEMAG for a 3% SDR (Fig. 21b). Considering that this drift level is relatively large in seismic design of structures, the configuration of SP2-9ST12-B12 can also be considered adequate to meet the performance objectives of NBB design. The application of rib stiffeners for a brace length equal to approximately two-thirds of its total length appears to be effective for this specimen, too. However, as it was stated before, a further investigation is required to validate this finding considering as a parameter the length of the brace. Fig. 21d compares the cyclic lateral load – SDR relation between the SP2-9ST12-B18 and the non-strengthened SP2 model. As shown in this comparison, local buckling can be completely prevented under the five repeated cycles of 1.5% SDR, while the growth of local buckling can be efficiently reduced up to a 3.0% SDR using sufficiently thick stiffeners (i.e., 12 mm) and battens (i.e., 18 mm), thus providing a very stable hysteretic behaviour up to high inelastic levels.

5. Hysteretic model and energy dissipation performance of NBB tests

5.1. Hysteretic model of chevron NBBs

In real-world applications, it is preferred to use braces as a pair [18] to balance the difference in tensile and compressive behaviour. In this section, the hysteretic model of NBBs arranged as chevron configuration is developed. The proposed model is presented in Fig. 22. On the basis of the backbone curve equations introduced in the Section 2.2, the stiffness and strength in Fig. 22 can be expressed as follows:

$$K_1 = 2K_e H \cos^2 \theta \tag{11}$$

$$P_1 = 2P_{y,LY} \cos \theta \tag{12}$$

$$K_2 = K_{p,ave} H \cos^2 \theta \tag{13}$$

$$P_2 = \left(P_{y,LY} + P_{y,HS}\right) \cos \theta \tag{14}$$

$$K_3 = K_e H \cos^2 \theta \tag{15}$$

where H is the story height (in this paper, 2600mm which is the distance between the inner sides of top and bottom beams), θ is the installation angle of NBB (45º in this study).
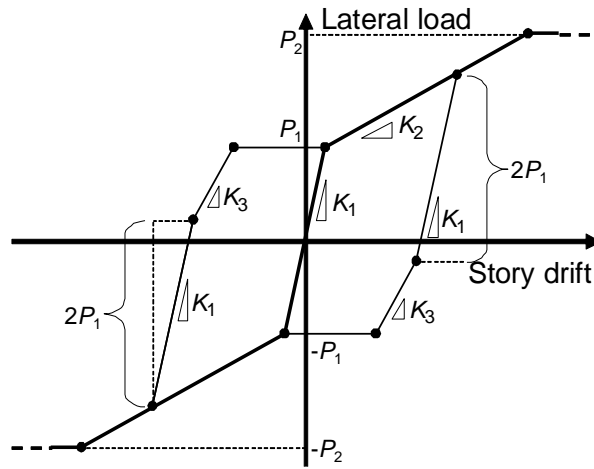

Fig. 22. Hysteretic loop of chevron NBBs

Fig. 23 compares the test results with the proposed hysteretic analytical model. The vertical axis refers to the lateral forces, while the horizontal axis to the SDR. The test results shown by the solid gray line are based on the hysteretic response obtained from the test campaign until a 2% SDR. Until the onset of local buckling, the proposed model conservatively estimates the test results. In both specimens, the proposed model underestimates the test result at the proximity of the beginning of the second stiffness range. This may be attributed to the effect of relatively high isotropic hardening of LYS [39] as well as the increase of the yield stress due to the cold forming of both channels [42]. The whole calculation process of the hysteretic model is provided in the Appendix.
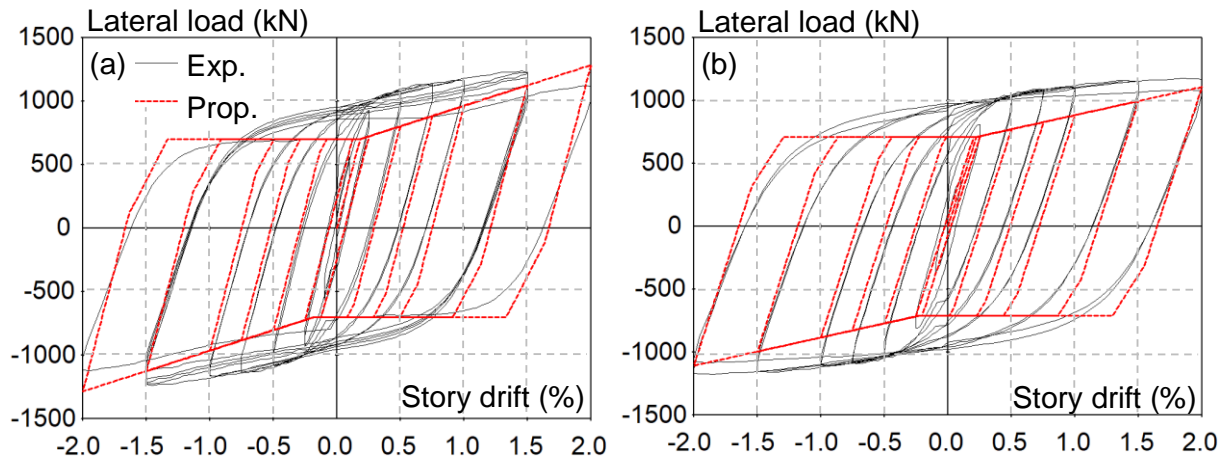
Fig. 23. Lateral force – story drift relation of chevron NBBs; (a) Specimen 1, (b) Specimen 2

5.2. Energy dissipation performance, ξ_{eq}

Utilizing the test results, the equivalent viscous damping ratio of chevron NBBs is computed. Fig. 24 shows the ξ_{eq} values computed at each amplitude. In both specimens, energy dissipation is observed from small story drifts. At 0.75% SDR, ξ_{eq} value exceeds 0.3 and reaches 0.4 after 1.5% SDR which is a quite high value for a bracing system. The capacity of the proposed steel braces to dissipate large quantities of energy, in some cases even in response to very small story drifts, is notable, thanks to the combined axial-flexural behaviour and use of LYS.
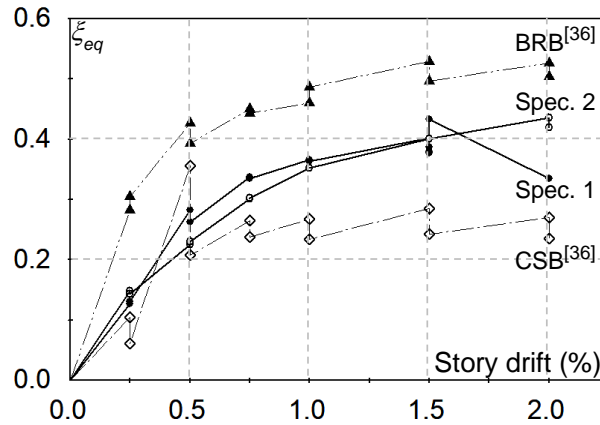

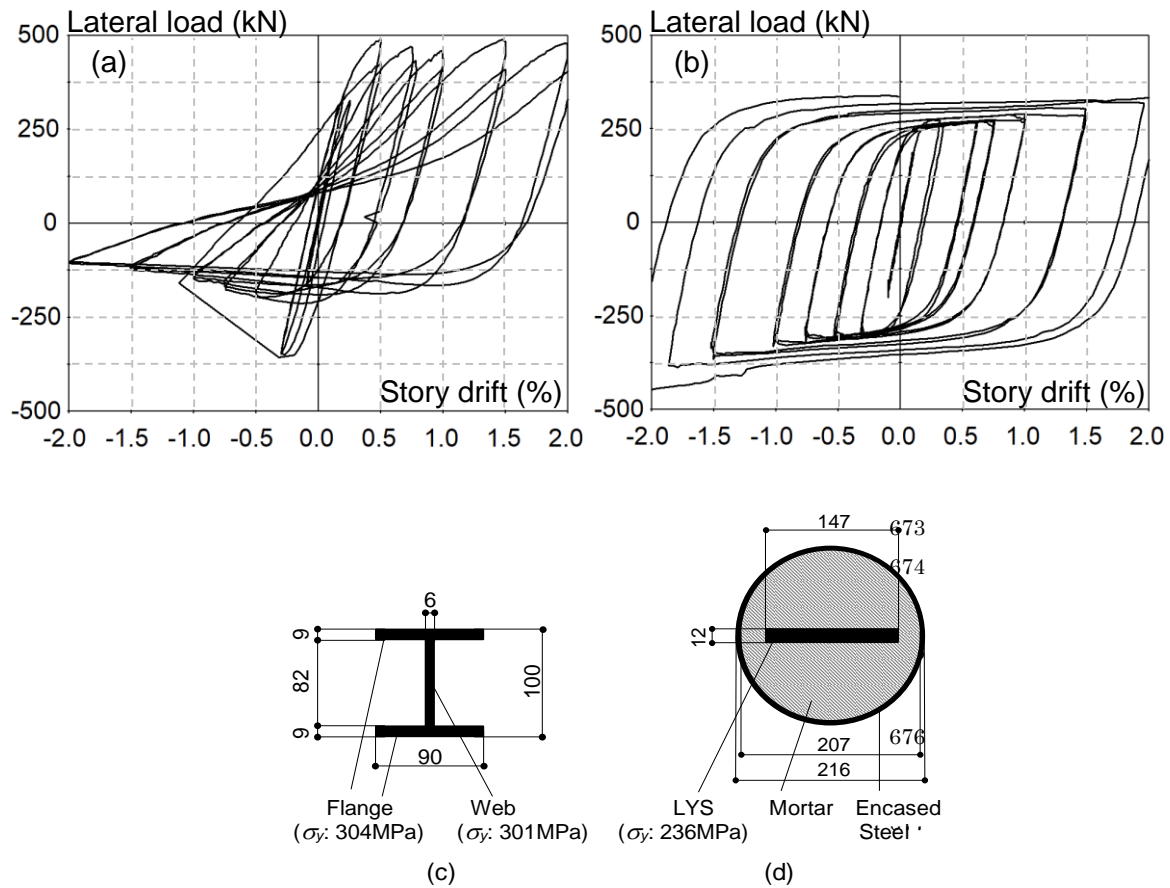**Fig. 24.** Equivalent viscous damping computed at each story drift

Fig. 25. Lateral force – story drift relation of single (a) CSB and (b) BRB specimens; Cross-sections and materials of (c) CSB and (d) BRB specimens.

The ξ_{eq} of NBBs is compared with that of a conventional steel brace (CSB) and a buckling restrained brace (BRB). The results are shown in Fig. 24. The CSB and BRB specimens have been tested by the authors and co-workers in a previous research work and details of this work can be found elsewhere [43]. It should be noted that these tests were performed under a quasi-static cyclic loading protocol, similar with the one adopted in the present experimental work of NBBs with the only difference being that all loading cycles were repeated two times. The cyclic behaviour of the CSB and BRB specimen is shown in Fig. 25a and Fig. 25b, respectively (single brace test). The slenderness ratio of CSB specimen is 54.0 defined about the weak axis. Details of the CSB and BRB cross-sections are shown in Fig. 25c and d, respectively. The ξ_{eq} of both the CSB and BRB has been calculated considering chevron configuration as in the calculation of ξ_{eq} for NBBs. By comparing the ξ_{eq} of all brace specimens, BRB and NBB exhibit a higher energy dissipation performance compared to CSB. NBB exhibits a lower ξ_{eq} than the BRB specimen because of its higher post-yielding stiffness. As this can be explained through the definition of ξ_{eq}, a hysteretic behaviour with high post-yielding stiffness naturally leads to a smaller ξ_{eq} when compared with systems of almost no post-yielding stiffness (e.g., BRB specimen) [41]. Moreover, LYS was utilized in the fabrication of the yielding core of the BRB specimen, thereby a very "fat" hysteretic loop is observed in BRB swollen by the high isotropic hardening of the LYS.

6. Conclusions

In this research, the cyclic behaviour of Naturally Buckling Braces (NBB) was investigated through full-scale testing and computational simulations. Two different specimens with intentional eccentricity were tested to evaluate the cross-sectional size and influence of eccentricity on the brace performance.

A finite element (FE) model was prepared in ABAQUS software to conduct a parametric study for exploring various strengthening methods of NBB's built-up section against local buckling and cumulative damage. The use of sufficiently thick stiffeners and battens can strengthen NBB's energy dissipation capacity up to high inelastic levels, indicating that NBB shall be used as a reliable damping system. An analytical formula for modeling the hysteretic behaviour of NBB in chevron configuration is also proposed and validated with the test results. Main conclusions are as follows:

- The two full-scale test specimens exhibited a stable behaviour without any fracture or substantial strength deterioration up to a 1.5% story drift ratio (SDR). The specimen with larger steel section and eccentricity designed for higher ductility demands showed high plastic deformation capacity with small amount of tensile strength deterioration even after the completion of 5 repeated loading cycles of 2% SDR. The brace retained 94% of the tensile force reached in the first tensile cycle of the repeated loading.

- In order to enhance member's strength as well as its energy dissipation performance, asymmetric full-scale built-up sections that employ a thicker low-yield-point steel (LYS) channel than the counterpart high-strength steel (HSS) channel was proposed. Test result suggested that although the hysteretic behaviour of such steel section configuration behaved as expected, local buckling was triggered at a smaller SDR (i.e., 1.5% or 2.0%) compared to the corresponding half-scale specimens with symmetrical built-up section (i.e., 3.0%). This is because the centroid of the asymmetrical section moves towards the LYS channel centroid, thus reducing the effective intentional eccentricity. The onset of local buckling in full-scale specimens at an earlier SDR than in half-scaled specimens is also related to the size effect.

- The proposed in-plane gusset-plate connection behaved like an ideal pinned connection allowing the bracing system to develop its beneficial high post-yielding stiffness and ductile behaviour. After brace ends reached a maximum rotation of 0.12 rad, no cracks or fracture was observed in the gusset-plate connections.

- The application of rib stiffeners in the steel sections for a central length approximately equal to the two-thirds of the total brace length was found to be beneficial based on the FE results. About 40% increase of the energy dissipating capacity at a 2% SDR was observed in the rib strengthened NBBs compared to the non-strengthened NBBs. Specimen 1, which has an effective eccentricity over cross-sectional radius of gyration (e''/r_{com}) equal to 1.23 and a slenderness ratio equal to 44, requires at least 9 stiffeners and channel battens of 12 mm thickness. Specimen 2, which has an e''/r_{com} equal to 1.63 and a slenderness ratio equal to 37.9, requires at least 9 stiffeners and channel battens of 12 mm or 18 mm thickness.

- By comparing the equivalent damping ratio, and the maximum and cumulative strain curves for the FE models with various number of stiffeners, thickness of stiffeners and thickness of battens, it can be concluded that the number of rib stiffeners has the greatest impact on the cyclic behaviour of NBB, followed by the thickness of battens. The thickness of rib stiffeners has the smallest influence on the energy dissipation capacity of NBB but rib stiffeners of at least 9 mm thickness shall be used for the NBB section with channel width-to-thickness ratio $B/t_{LY} = 13.6$ and at least 12 mm thickness for $B/t_{LY} = 16.0$. Based on FE analysis results, local buckling can be reduced up to a SDR equal to 3% in strengthened full-scale NBBs.

- The proposed hysteretic model estimated the test results of full-scale specimens with relatively good accuracy and in a conservative way. Since the equations in the literature are based on the result of scaled specimens, size effect is considered as negligible for the backbone or hysteresis estimation. It should be noted that, in order to avoid overestimation of the strength in compression, prevention of buckling in the LYS steel channel is essential at least for the target SDR.

- The test specimens provided an equivalent damping coefficient ξ_{eq} equal to 0.3 at 0.75% SDR. The ξ_{eq} further increased and reached a value of 0.4 after 1.5% SDR. This value is larger than what is typically observed in conventional steel braces and lower than what is observed in buckling restrained braces. NBB is deemed to provide an efficient energy dissipation capacity as a lateral load resistant system for braced frame structures.

CRediT authorship contribution statement

Declaration of competing interest

The authors declare that they have no known competing financial interests or personal relationships that could have appeared to influence the work reported in this paper.

Acknowledgement

References

[1] López W.A. and Sabelli R. Seismic design of buckling-restrained braced frames. Steel Tips Series, Structural Steel Educational Council 2004, USA.

[2] Shibata M, Nakamura T. and Wakabayashi M. Mathematical expression of hysteretic behavior of braces: Part 1 Derivation of hysteresis functions. Transactions of AIJ 1982; 316:18-24. (in Japanese)

[3] Takeuchi T. and Matsui R. Cumulative cyclic deformation capacity of circular tubular braces under local buckling. J Struct Eng ASCE 2011;137(11):1311-1318.

[4] Tremblay R. Inelastic Seismic Response of Steel Bracing Members. J Constr Steel Res 2002;5-8(58):665-701.

[5] Miller D.J, Fahnestock L.A. and Eatherton M.R. Development and experimental validation of a nickel–titanium shape memory alloy self-centering buckling-restrained brace. Eng Struct 2012; 40:288–298.

[6] Tremblay R., Lacerte M. and Christopoulos C. Seismic response of multistory buildings with self-centering energy dissipative steel braces. J Struct Eng 2008;134(1):108–120.

[7] Kumar G.R., Kumar S.R.S. and Kalyanaraman V. Behaviour of frames with non-buckling bracings under earthquake loading. J Constr Steel Res 2007;63(2):254–262.

[8] Sabelli R., Mahin S. and Chang C. Seismic demands on steel braced frame buildings with buckling-restrained braces. Eng Struct 2003;25(5):655–666.

[9] Black C., Makris N. and Aiken I. Component testing, stability analysis and characterization of buckling-restrained unbonded braces. PEER Report 2002/08. Pacific Earthquake Engineering Research Center, University of California, Berkeley, September 2002.

[10] Guerrero H., Escobar A.J., Teran-Gilmore A. Experimental damping on frame structures equipped with buckling-restrained braces (BRBs) working within their linear-elastic response. Soil Dyn Earth Eng 106: 196–203

[11] Takeuchi T., Suzuki K., Ida M. and Yamada S. Estimation of cumulative deformation capacity of buckling restrained

794   braces. J Struct Eng ASCE 2008; 134(5): 822-831.

795 [12] Ji X., Kato M., Wang T., Hitaka T. and Nakashima M. Effect of gravity columns on mitigation of drift concentration for
796   braced frames. J Constr Steel Res 2009;12(65):2148–2156.

797 [13] Wang H., Feng Y., Wu J., Jiang Q. and Chong X. Deformation concentration effect of multistory buckling restrained
798   braced frames. Advances in Civil Eng 2019; Article ID 7164373. https://doi.org/10.1155/2019/7164373.

799 [14] Veismoradia S., Cheraghia A., Darvishan E. Probabilistic mainshock-aftershock collapse risk assessment of buckling
800   restrained braced frames, Soil Dyn Earth Eng 2018; 115: 205-216.

801 [15] Hsiao P.C., Hayashi K., Inamasu H., Luo Y.B. and Nakashima M. Development and testing of naturally buckling steel
802   braces, J Struct Eng ASCE 2016;1(142).

803 [16] Inamasu H., Hsiao P.C., Hayashi K. and Nakashima M. Development and experiment of naturally buckling brace
804   combining different types of steel material. Transactions of AIJ 2015; 713:1165-1174. (in Japanese)

805 [17] Inamasu H., Skalomenos K.A., Hsiao P.C., Hayashi K., Kurata M. and Nakashima M. Gusset plate connections for
806   naturally buckling braces, J Struct Eng ASCE 2017;8(143).

807 [18] Inamasu H., Skalomenos K.A., Shimada H., Kurata M. and Nakashima M. Physical model and numerical investigation
808   of seismic performance of naturally buckling brace. H28 AIJ Kinki conference 2016;56:433-436. (in Japanese)

809 [19] Skalomenos, K. A., Inamasu, H., Shimada, H., and Nakashima, M. Development of a steel brace with intentional
810   eccentricity and experimental validation. J Struct Eng ASCE 2017;8(143).

811 [20] Hsiao P.C. and Lin K.S. Slenderness effects in naturally buckling braces under seismic loads. J Struct Eng ASCE
812   2020;165(5): 04020058

813 [21] Hsiao P.C. and Cheng Y.T. Effects of far-field and near-fault cyclic loadings on seismic performance of naturally
814   buckling braces in pairs. Eng Struct 2020;214.

815 [22] Skalomenos K.A., Kurata M., Shimada H., Nishiyama M. (2018), Use of induction heating in steel structures: material
816   properties and novel brace design, Journal of Constructional Steel Research 2018, 148: 112–123,
817   https://doi.org/10.1016/j.jcsr.2018.05.016

818 [23] Skalomenos K.A., Kurata M., Nishiyama M., Induction-heat treated steel braces with intentional eccentricity,
819   Engineering Structures 2020, 211: 110461, https://doi.org/10.1016/j.engstruct.2020.110461

820 [24] Bazant Z.P. Size effect. International Journal of Solids and Structures 2000; 37:69-80.

821 [25] Bazant Z.P. Size effect on structural strength: A review. Archive of Applied Mechanics 1999; 69:703-725.

822 [26] Zheng Li and Pasternak H. Statistical size effect of flexural members in steel structures. J Constr Steel Res
823   2018;144:176-185.

824 [27] Fell B.V., Kanvinde A.M., Deierlein G.G., Myers A.T. and Fu X. Buckling and fracture of concentric braces under
825   inelastic cyclic loading. Steel Technical Information and Product Service Report (Steel TIPS) 2006. Structural Steel
826   education Council, Moraga, CA.

827 [28] Li W., Wu B., Ding Y. and Zhao J. Experimental performance of buckling restrained braces with steel cores of H-
828   section and half-wavelength evaluation of higher-order local buckling. Advances in Struct Eng 2017;20(4):641–657.

829 [29] Matsui R., Takeuchi T., Hajjar J.F., Nishimoto K. and Aiken I. Local buckling restraint condition for core plates in
830   buckling restrained braces. J Constr Steel Res 2010;66:139–149. https://doi.org/10.1016/j.jcsr.2009.09.002.

831 [30] Mulligan, G.P. and Teoman P. The influence of local buckling on the structural behavior of singly symmetric cold-
832   formed steel columns. Center for Cold-Formed Steel Structures Library 1983;117. https://scholarsmine.mst.edu/ccfss-
833   library/117.

834 [31] Azhari M. and Bradford M.A. Local buckling of I- Section beams with longitudinal web stiffeners. Thin-walled
835   structures 1993;15:1-13.

836 [32] Fujikubo M. and Yao T. Elastic local buckling strength of stiffened plate considering plate/stiffener interaction and
837   welding residual stress. Marine Structures 1999;12:543-564.

838 [33] Li L.Z., Jiang C.J., Jia L.J. and Lu Z.D. Local buckling of bolted steel plates with different stiffener configuration.
839   Engineering Structures 2016;119:186–197.

840 [34] American Institute of Steel Construction (AISC). Seismic provisions for structural steel building. AISC/ANSI Standard
841   2016;341:16.

842 [35] American Institution of Steel Construction (AISC). Specification for structural steel buildings. AISC/ANSI Standard

843   2016;360:16.

[36] Scozzese F., Terracciano G., Zona A., Corte G.D., Dall'Asta A., Landolfo R. Analysis of seismic non-structural damage in single-storey industrial steel buildings 2018. Soil Dyn Earth Eng 114: 505–519

[37] Okazaki, T., Lignos, D. G., Hikino, T., and Kajiwara, K. Dynamic response of a chevron concentrically braced frame. J Struct Eng ASCE 2013;4(139):515–525.

[38] Smith M. ABAQUS/Standard User's Manual, Version 2016. Dassault Systèmes Simulia Corp, Providence, RI.

[39] Nakashima M. Strain hardening behavior of shear panels made of low-yield steel Part I: Test. J Struct Eng ASCE 1995;121(12).

[40] Hudson D.E. Equivalent viscous friction for hysteretic systems with earthquake-like excitations: Proceedings of the 3rd World Conference on Earthquake Engineering, vol II, 185–202; 1965

[41] Chopra, A.K. Dynamics of structures: Theory and applications to earthquake engineering, 4th Edition. Prentice Hall: Englewood Cliffs, NJ; 2012.

[42] MacDonald M., Rhodes J., Crawford M. and Taylor G.T. A study on the effect of cold forming on the yield strength of stainless steel - Hardness test approach. International specialty conference on cold-formed steel structures, St. Louis, Missouri, U.S.A., October 17-18,1996.

[43] Special project for reducing vulnerability for urban mega earthquake disasters (ii) Maintenance and recovery of functionality in urban infrastructures. H26 report 2015;143-152. (in Japanese) http://www.toshikino.dpri.kyoto-u.ac.jp/report/2014/report_j_2014.html.

Appendix

Calculation of section property and hysteretic loop of full-scale NBB specimens tested in this paper is summarized as follows.

A.1. Primary property : Specimen 1, Specimen 2

HSS channel cross-sectional area A_{HS} : 2,253 mm^2, 2,687 mm^2

LYS channel cross-sectional area A_{LY} : 2,819 mm^2, 3,430 mm^2

Steel Young's modulus E : 205,000 MPa

Distance between brace center and the line of force action $e^{\#}$: 85 mm, 130 mm

Initial eccentricity e'': 78.7 mm, 121.8 mm

Eccentricity of HSS channel only e : 148.6 mm, 203.3 mm

Radius of gyration r_{com} : 64.2 mm, 74.6 mm

Brace effective length L : 2,825 mm

Section modulus S_{com} : 292,121 mm^3, 411,735 mm^3

HSS yield stress $s_{y,HS}$: 638 MPa

LYS yield stress $s_{y,LY}$: 231 MPa

$P_1 = 2P_{y,LY}\cos\theta = 700$ kN, 711 kN

$P_2 = \left(P_{y,LY} + P_{y,HS}\right)\cos\theta = 1,964$ kN, 2,315 kN

LYS ultimate stress $s_{u,LY}$: 308 MPa

A.2. Backbone calculation : Specimen 1, Specimen 2

$$K_e = \frac{E(A_{LY}+A_{HS})/L}{1+(e''/r_{com})^2} = 147,067 \text{ N/mm},\quad 120,837 \text{ N/mm}$$

$$P_{y,LY} \cong P_c = \frac{\sigma_{y,LY}(A_{LY}+A_{HS})}{1+e''(A_{LY}+A_{HS})/S_{com}} = 495 \text{ kN},\quad 503 \text{ kN}$$

$$C_1 = \{-0.0045(e''/r_{com}) + 0.024\}(L/r_{com}) = 0.814,\quad 0.631$$

$$C_2 = \{-0.45(e''/r_{com}) + 1.75\}\left(\sigma_{y,HS}/\sigma_{y,LY}\right)^{-0.5} = 0.721,\quad 0.611$$

$$K_{p1} = \frac{EA_{HS}/L}{1+\{e/(C_1 r_{com})\}^2} = 17,995 \text{ N/mm},\quad 9,908 \text{ N/mm}$$

888 $\quad K_{p2} = \dfrac{EA_{HS}/L}{1+\{C_2 e/(C_1 r_{com})\}^2} = 31{,}393$ N/mm, $\;$ 24,487 N/mm

889 $\quad K_{p,ave} = (K_{p1} + K_{p2})/2 = 24{,}694$ N/mm, $\;$ 17,198 N/mm

890 $\quad P_{y,HS} = \sigma_{u,LY} A_{LY} + \sigma_{y,HS} A_{HS} = 2{,}283$ kN, $\;$ 2,771 kN

891

892 $\quad$ *A.3. Hysteresis loop calculation $:$ Specimen 1, Specimen 2*

893 $\quad K_1 = 2K_e H \cos^2 \theta = 1{,}911$ kN/%, $\;$ 1,570 kN/%

894 $\quad K_2 = K_{p,ave} H \cos^2 \theta = 321$ kN/%, $\;$ 224 kN/%

895 $\quad K_3 = K_e H \cos^2 \theta = 956$ kN/%, $\;$ 785 kN/%